

Massive Molecular Outflows Associated with UCHII/HII Regions

Sheng-Li, Qin^{1,2}; Jun-Jie, Wang¹; Gang Zhao¹; Martin, Miller³ and Jun-Hui, Zhao²

¹ National Astronomical Observatories, Chinese Academy of Sciences, Beijing 100012, P. R. China

² Harvard-Smithsonian Center for Astrophysics, 60 Garden Street, Cambridge, MA 02138, USA

³ I.Institute of Physics, University of Cologne, Cologne, 50937, Germany

Received date ; Accepted date

Abstract. Aims: We searched for the molecular outflows from fifteen molecular clouds associated with ultra-compact and compact HII (UCHII/HII) regions and discussed possible gas heating mechanism. Methods: Mapping observations of CO $J = 3 - 2$ and $J = 2 - 1$ lines were carried out with the KOSMA 3m-Telescope towards the 15 HII region/molecular cloud complexes. Results: Ten molecular outflows were identified out of the fifteen HII region/molecular cloud complexes. Higher outflow detection rate (67%) suggested that the outflows are common in high mass star forming regions as those in low mass star forming regions, which is consistent with the results constructed by the other authors. The observations also showed that the outflow might occur in the stage of HII region. The integrated CO line intensity ratios ($R_{\text{CO}(3-2)/\text{CO}(2-1)}$) were determined from the core component of the spectra as well as from both the blue and red wings. Maximum line intensity ratios from the wings and core components appeared to be related to the mid-infrared sources imaged by Midcourse Space Experiment (MSX). The relationship between the maximum line intensity ratios and MSX sources appears to indicate that the molecular gas could be heated by the emission of dust associated with massive stars. Based on maser observations reported in the literatures, we found that H₂O masers were only detected in seven regions. The H₂O masers in these regions are located near the MSX sources and within the maximum line intensity ratio regions, suggesting that H₂O masers occur in relatively warm environments.

Key words. stars:formation–stars:early-type–ISM:HII regions–ISM: outflows

1. Introduction

Ultra-compact and compact HII regions provide the information about the massive star formation within molecular clouds (Heyer et al. 1989; Churchwell 2002). The dust surrounding the massive stars or HII regions absorbs nearly all the stellar radiation and re-radiates at the far-infrared and mid-infrared bands (e.g. Wood & Churchwell 1989; Churchwell 2002). The molecular clouds associated with HII regions have higher ratio of CO $J = 3 - 2$ to CO $J = 2 - 1$ and have higher gas temperature than those sources without HII regions (Wilson, Walker & Thornley 1997). The high gas temperature of molecular clouds might be related to the warm dust components associated with the HII regions (Kaufman et al. 1999; Goldreich & Kwan 1974). Various kinds of masers have been also detected frequently in massive star formation regions. Different masers maybe occur in different astrophysical environments. For example, both observations and theoretical models suggested that H₂O masers originate in hot cores, and are excited by the shocks associated with outflows or accretion (Elitzur, Hollenbach & McKee 1989; Felli, Palagi & Tofani 1992; Codella, Testi & Cesaroni

1997; Garay & Lizano 1999). Molecular outflows have been found from the regions associated with all kinds of protostars, which are considered as a good indicator of star formation (Beuther et al. 2002; Shepherd & Churchwell 1996a, 1996b; Bachiller 1996; Bontemps et al. 1996; Wu et al. 2004, 2005). In the process of massive star formation, the molecular outflows appeared to be a common phenomenon in the early stages prior to UCHII regions (e.g. Beuther et al. 2002) and of UCHII regions (e.g. Shepherd & Churchwell 1996b). However, it has not been fully understood that how the outflows initially start from HII regions and what kinds of link between HII regions and molecular clouds in large scale structures. Aiming at understanding the relationship between massive stars and those associated astrophysical phenomena, we carried out observations of CO $J = 3 - 2$, $J = 2 - 1$ and ¹³CO $J = 2 - 1$ towards fifteen HII region/molecular cloud complexes. The sources were selected from the sample of HII regions which have been detected at 1.46 and 5.89 GHz by VLA (Fich 1993) and the catalog of UCHII regions that were compiled by Kurtz, Churchwell & Wood (1994). Comparing to the sources of Beuther et al. (2001) and Shepherd & Churchwell (1996b), all these fifteen sources in this sample have H_α emission from the red plate of

the Palomar Observatory Sky Survey (POSS)¹ and are in relatively evolved stage. Although the sources in our sample are not statistically completed, the observations illustrate the massive star forming and molecular gas properties associated with HII regions.

The different transitions of CO trace different molecular environments. For example, the CO $J = 3 - 2$ and CO $J = 2 - 1$ transitions have distinct upper energy level temperatures and critical densities. The upper energy level temperature and critical density in CO $J = 2 - 1$ line are 16.6 K and about 10^4 cm^{-3} while those for CO $J = 3 - 2$ line are 33.2 K and $5 \times 10^4 \text{ cm}^{-3}$ (Kaufman et al. 1999). Therefore, the ratio of line intensities between CO $J = 3 - 2$ and CO $J = 2 - 1$ indicates the temperature and density structure of molecular cloud environments if the molecular gas is optically thin (Hasegawa et al. 1994; Wilson, Walker & Thornley 1997). Previous studies have showed that the emission of CO ($J = 3 - 2$ and $J = 2 - 1$) in line wings and line center is optically thick in star formation regions (Choi, Evans II & Jaffe 1993; Correia, Griffin & Saraceno 1997; Langer & Penzias 1990). According to Wilson et al. (1997, 1999) and Kim & Koo (2002), the line intensity ratios based on the optically thick CO transitions indicate that the temperature varies at different positions. The mid-infrared emission at $8.3 \mu\text{m}$ is thought to be from small dust grains and polycyclic aromatic hydrocarbons (PAHs), and be excited by the UV radiation leaking from the HII regions (Leger & Puget 1984; Deharveng et al. 2003, 2005). The radio continuum at 1.4 GHz from NRAO VLA Sky Survey (NVSS)² have angular resolution of $45''$ and the sensitivity of 45 mJy (Condon et al. 1998). The Midcourse Space Experiment (MSX) band A (at $8.3 \mu\text{m}$) emission was imaged at angular resolution of $18.3''$ with the sensitivity³ of 0.1 Jy. The relationship of gas temperature traced by line intensity ratio, warm dust traced by $8.3 \mu\text{m}$ emission and radio continuum at 1.4 GHz will be discussed in this paper.

In this paper, we report the results from the observations of the fifteen HII regions at the CO $J = 3 - 2$ and CO $J = 2 - 1$ transitions using KOSMA (Kölner Observatorium für Sub-Millimeter Astronomie)⁴ at mm/submillimeter wavelengths. We also observed $^{13}\text{CO } J = 2 - 1$ for six sources. The rest of the paper is outlined here. In section 2, the observations are described. The results from the observations are given in section 3. Possible mechanisms driving the outflows and the gas heating are discussed in section 4. Section 5 summarizes the results.

2. Observations & Data Reduction

We carried out the observations toward fifteen HII region/molecular cloud complexes in CO $J = 3 - 2$ and CO $J = 2 - 1$ lines (345.796 and 230.538 GHz) using the KOSMA

3m telescope at Gornergrat, Switzerland, between February and April 2004. The dual-channel 230/345 GHz SIS receivers (Graf et al. 1998) were used to simultaneously observe the two transitions of CO. DSB receiver noise temperatures were about 120 K. In addition, $^{13}\text{CO } J = 3 - 2$ and $2 - 1$ lines at the rest frequencies of 330.588 and 220.399 GHz were also observed toward 6 sources in this sample. The integration time on the sources appeared not long enough to derive significant results from $^{13}\text{CO } J = 3 - 2$ data at 330.588 GHz.

The medium and variable resolution acousto optical spectrometers (Schieder et al. 1989) with 1501 and 1601 channels or bandwidth of 248 and 544 MHz at 230 and 345 GHz were used as backends. The channel widths of 165 and 340 kHz correspond to velocity resolutions of 0.21 and 0.29 km s^{-1} at 230 and 345 GHz which result in different rms noise levels of T_{mb} in each channel as shown in Table 1, respectively. The beam size and main beam efficiency were determined using continuum cross scans on Jupiter. The beam sizes at 230 and 345 GHz were $130''$ and $80''$, respectively. The forward efficiency F_{eff} was 0.93 during our observations. The corresponding main beam efficiencies B_{eff} were 0.68 and 0.72 at 230 and 345 GHz, respectively. Pointing was frequently checked on Jupiter and better than $20''$. Table 1 summarizes observations. In Table 1, Table 2, Table 3 and Table 4, G139, G206, G189, G213, G192 and G70 represent G139.909+0.197, G206.543-16.347, G189.876+0.516, G213.880-11.837, G192.584-0.041 and G70.293+1.600, respectively. The six sources are from Kurtz, Churchwell & Wood (1994), and the other nine sources are from Fich (1993).

All the maps were made using on-the-fly mode with $1' \times 1'$ grid, except for G70.293 with a $2' \times 2'$ grid. The sources were scanned along the right ascension (RA) at a fixed declination (Dec) with a constant integration time of 4 second at each point. The sky level was taken out by observing the off-source position in real time. Then, the scan continued by moving to next row of the grids. We repeated the observing procedure 6 times over the entire source. The data were integrated at each point in order to obtain high S/N ratio. The data reduction was carried out using the Continuum and Line Analysis Single-Disk Software (CLASS) and Grenoble Graphic (GREG) software packages. A least-square fit to baselines in the spectra was carried out with the first order polynomial. The baseline slopes were taken out for all the sources. The correction for the line intensities to main beam temperature scale was made using the formula $T_{\text{mb}} = (F_{\text{eff}}/B_{\text{eff}})T_{\text{A}}^*$.

3. Analysis and Results

For those sources with broad wings, we first drew position-velocity (P-V) diagrams. According to the P-V diagrams, we selected the integrated range of wings and determined the outflow intensities of red and blue lobes. Ten molecular outflows were identified by the contours of integrated intensities of CO $J = 2 - 1$ line wings. The molecular cloud cores in CO $J = 2 - 1$ line for the sources with and without outflows were also imaged. The molecular cores in $^{13}\text{CO } J = 2 - 1$ line for the six sources were imaged with the same integrated velocity range as those in CO $J = 2 - 1$ line. The velocity intervals and

¹ Available at <http://archive.stsci.edu/dss/>

² Available at <http://www.cv.nrao.edu/nvss/postage.shtml>.

³ Available at <http://iras.ipac.caltech.edu/applications/MSX/>.

⁴ The KOSMA 3m telescope is operated at submillimeter wavelengths by the University of Cologne in collaboration with Bonn University.

the maximum integrated intensities for the maps are summarized in Table 2. In order to obtain the intensity ratio of CO $J = 3 - 2$ to CO $J = 2 - 1$ lines, we convolved the $80''$ resolution of CO $J = 3 - 2$ data with an effective beam of size $\sqrt{130^2 - 80^2} = 102''$. The integrated intensities were calculated for CO $J = 3 - 2$ line in the same velocity range as for CO $J = 2 - 1$. The ratio $R_{I_{\text{CO}(3-2)}/I_{\text{CO}(2-1)}}$ of the integrated line intensity in CO was determined from the core component of the spectra as well as from both the blue and red wings.

Assuming the CO $J = 2 - 1$ emission in the line wings is optically thin, and taking the upper energy level temperature 16.6 K as excitation temperature, the column densities of line wings within one beam were calculated using the equation 1 (Garden et al. 1991). If we assume the CO abundance $[\text{CO}]/[\text{H}_2] = 10^{-4}$ and the mean atomic weight of the gas $\mu_g = 1.36$, the outflow mass, the momentum, the kinetic energy within one beam were derived using equations 2-4 (cf. Goldsmith et al. 1984),

$$N_{\text{CO}} = 1.08 \times 10^{13} \frac{T_{\text{ex}}}{\exp(-16.6/T_{\text{ex}})} \int T_{\text{mb}} dv \text{ (cm}^{-2}\text{)}, \quad (1)$$

$$M_i = 7.94 \times 10^{-4} D^2 \frac{T_{\text{ex}}}{\exp(-16.6/T_{\text{ex}})} \int T_{\text{mb}} dv \text{ (M}_{\odot}\text{)}, \quad (2)$$

$$P_i = 7.94 \times 10^{-4} D^2 \frac{T_{\text{ex}}}{\exp(-16.6/T_{\text{ex}})} \int T_{\text{mb}} v dv \text{ (M}_{\odot} \text{ km s}^{-1}\text{)}, \quad (3)$$

$$E_i = 7.90 \times 10^{39} D^2 \frac{T_{\text{ex}}}{\exp(-16.6/T_{\text{ex}})} \int T_{\text{mb}} v^2 dv \text{ (erg)}, \quad (4)$$

where v in km s^{-1} is the velocity of the gas with respect to the cloud systemic velocity and $T(v)$ in K is the brightness temperature at v ; D is the distance from the Sun in kpc; the subscript i indicates the observed points within the outflow zone. By summing up the values at all the observed points in the red and blue lobes, the outflow mass M , the momentum P , the kinetic energy E were obtained.

The timescale t , the characteristic velocity V , the mass loss rate \dot{M}_{loss} , the driving force F and mechanical luminosity L_m were derived using the equations below (cf. Goldsmith et al. 1984),

$$V = \frac{P}{M} \text{ (km s}^{-1}\text{)}, \quad (5)$$

$$t = 9.78 \times 10^5 \frac{R}{V} \text{ (yr)}, \quad (6)$$

$$\dot{M}_{\text{loss}} = \frac{P}{tV_w} \text{ (M}_{\odot} \text{ yr}^{-1}\text{)}, \quad (7)$$

$$F = \frac{P}{t} \text{ (M}_{\odot} \text{ km s}^{-1} \text{ yr}^{-1}\text{)}, \quad (8)$$

$$L_m = 8.28 \times 10^{-42} \frac{E}{t} \text{ (L}_{\odot}\text{)}, \quad (9)$$

where R in pc is the outflow size defined by the average of the the radius of the blue-shifted and red-shifted lobes, the wind velocity V_w is assumed to be 500 km s^{-1} (Martí, Rodríguez & Reipurth 1998). The physical parameters of the outflows are summarized in Table 3. Our results might only impose lower

limits on outflow parameters if line wings were optically thick and excitation temperature was larger than 16.6 K at CO $J = 2 - 1$ transition.

Using the formula of Casoli, Combes & Dupraz (1986), the far-infrared luminosities of IRAS sources associated with the HII regions in our sample were derived from the infrared flux densities at the 4 IRAS bands. The far-infrared luminosities of IRAS sources are summarized in Table 4. We went through the image of MSX band A towards the sources in our sample. The brightest emission at $8.3 \mu\text{m}$ is always centered at the MSX point-like sources and located near or at the same position as the IRAS sources/massive stars. G213.880-11.837 is out of the MSX survey. The emission at $8.7 \mu\text{m}$ in G213.880-11.837 centered at IRAS 06084-0611 was detected by Persi & Tapia (2003). The offset positions of the MSX sources from the associated IRAS source/massive stars are labeled in Figs.1-12 and presented in Table 4.

3.1. Outflows

The blue and red lobes of the outflows were mapped for all the outflow sources as shown in Figs.1-10 (see Appendix B). In each of the figures, the dot symbol marks the mapped points. The spectra averaged over the outflow zones are shown in the bottom-right panel.

3.1.1. S186

There are two IRAS sources, IRAS 01056+6251 and IRAS 01053+6251 within the HII region and molecular cloud complex S186. IRAS 01056+6251 is located near the center of the continuum at 1.4 GHz (NVSS) and 6 GHz (Fich 1993), which is a possible exciting source of the HII region S186. The derived far-infrared luminosity of IRAS 01053+6251 corresponds to a B3-type star. There is no radio continuum to be detected around IRAS 01053+6251. IRAS 01053+6251 appears to be a deeply embedded massive protostar.

In Fig. 1, the molecular core shows an elongated structure and extends in the direction of EW. The blue and red lobes of the outflow have a similar extension to the molecular core. The two MSX sources are located near the regions of the maximum line intensity ratio ($R_{I_{\text{CO}(3-2)}/I_{\text{CO}(2-1)}}$) determined from the core and wing components.

3.1.2. G139.909+0.197

G139.909+0.197 is located within the reflection nebula AFGL437, which is associated with IRAS 03035+5819. IRAS 03037+5819 is located about $2'$ NE of IRAS 03035+5819. IRAS 03035+5819 is located near the center of the NVSS continuum at 1.4 GHz. A bipolar outflow in the direction of NS has been observed in ^{12}CO (1-0) line (Arquilla & Goldsmith 1984). Gomez et al. (1998) suggested that the poor degree of collimation of the outflow may be due to the wind sweeping up the inhomogeneous molecular materials and creating a cavity or hollow in the bipolar lobes.

From the core diagram of Fig. 2, the line intensity ratio of $R_{I_{\text{CO}(3-2)}/I_{\text{CO}(2-1)}}$ decreases gradually from SE to NW. The MSX source near IRAS 03035+5819 is located near the region with maximum value of the line intensity ratio.

From Fig. 2, CO $J = 2 - 1$ line wing map shows that the morphology of the outflow is similar to that of CO $J = 1 - 0$ (Arquilla & Goldsmith 1984), but the size of outflow is less extended than that of Arquilla & Goldsmith. The result appeared to indicate that the outflow traced by CO $J = 2 - 1$ arises from warm layer closer to the central exciting star.

From the line intensity ratio map of the blue wing, the SiO maser 1 (Harju et al. 1998), H₂O masers 2, 3, 4 (Cesaroni, Palagi & Felli 1988; Palagi et al. 1993; Wynn-Williams et al. 1986), IRAS 03035+5819 and its associated MSX source are located within the maximum line intensity ratio region. SiO emission is known to be a tracer of shocks. The SiO maser 1 and H₂O masers 2, 3, 4 are located within the maximum line intensity ratio region, which is consistent with the model that H₂O masers are excited by shocks and associated with warm molecular environment (Elitzur, Hollenbach & McKee 1989; Felli, Palagi & Tofani 1992; Codella, Testi & Cesaroni 1997; Garay & Lizano 1999).

The line intensity ratio from the red lobe of the outflow correlates well with the MSX source near IRAS 03035+5819.

IRAS 03037+5819 and its associated MSX source are far away from the maximum line intensity ratio regions of both the wings and core components.

3.1.3. G189.876+0.516

G189.876+0.516 is associated with IRAS 06063+2040. There are three B-type stars (ALS 8745, ALS 8748 and HD 252325) in this HII region/molecular cloud complex. All of them are located south of IRAS 06063+2040. Both IRAS 06063+2040 and HD 252325 are associated with the NVSS continuum.

From core diagram of Fig. 3, the molecular cloud core has a compact structure stretching in NS direction, and bends toward west at 2' north of IRAS 06063+2040. The location of the massive stars and the distorted morphology of the molecular core may have been evidence for that the molecular cloud are squeezed by the stellar winds from stars ALS 8748 and HD 252325. The MSX source, IRAS source and ALS 8745 appear to be associated with a maximum $R_{I_{\text{CO}(3-2)}/I_{\text{CO}(2-1)}}$ region. However, a region with the maximum line intensity ratio, 2 arcmin NE of IRAS 06063+2040, has no identifications from the existing observations at IR/FIR/optical and radio continuum.

In Fig. 3, the morphology of the blue-shifted lobe of the outflow shows a similar structure to the NS extension of the molecular core, while the red lobe corresponds to the bent structure of the molecular core. In the blue-shifted lobe, the MSX source and IRAS source are located within the maximum $R_{I_{\text{CO}(3-2)}/I_{\text{CO}(2-1)}}$ region. However, the maximum $R_{I_{\text{CO}(3-2)}/I_{\text{CO}(2-1)}}$ from the red-shifted wing appears to be located along the NE edge of the red-shifted lobe.

3.1.4. G213.880-11.837

Cometary UCHII region G213.880-11.837 is located within the red nebula GGD14 and is associated with IRAS 06084-0611. H₂O maser (Rodriguze et al. 1980; Tofani, Felli & Faylor 1995) is located NE of IRAS 06084-0611. The NVSS continuum peaks at IRAS 06084-0611. The radio source VLA7 (Gomez et al. 1998) has a flux density of 0.17 mJy at 3.6 cm and is located at the H₂O maser region. The 8.7 μm and 12.5 μm images (Persi & Tapia 2003) have similar morphology to the radio counterparts observed at 2 cm and 3.6 cm from G213.880-

11.837 (Gomez et al. 1998, 2000). The similarity in morphology between Mid IR and radio continuum appears to show evidence for that ionized gas is mixed with the dust in the cloud.

In the core diagram of Fig. 4, the core contours of CO $J = 2 - 1$ and ¹³CO $J = 2 - 1$ have similar morphology to that of HCO⁺ $J = 1 - 0$ (Heaton et al. 1988). The map of $R_{I_{\text{CO}(3-2)}/I_{\text{CO}(2-1)}}$ shows a large intensity gradient from south to north. The H₂O maser and 8.7 μm emission are associated with the region with maximum line-intensity ratio.

From the outflow map of Fig. 4, the line intensity maps of the wing components show a highly collimated bipolar outflow. VLA7 is located at the axis of outflow and appears to be a signpost of the energy source of the outflow. The outflow extends in the direction of SE to NW and is perpendicular to the core of high density gas HCO⁺ $J = 3 - 2$ (Heaton et al. 1988). It is possible that the accretion disk traced by dense gas is responsible for the highly collimated bipolar outflow.

The maximum $R_{I_{\text{CO}(3-2)}/I_{\text{CO}(2-1)}}$ of the red wing is located at the head of red lobe of the outflow and is associated with the 8.7 μm emission and IRAS source. However, the H₂O maser is located within the maximum line intensity ratio region of the blue-shifted component and the maximum line intensity ratio is not associated with the 8.7 μm emission, suggesting that shocks may be responsible for the heating of CO gas in the blue lobe of the outflow.

3.1.5. G192.584-0.041

There are three IRAS sources (IRAS 06099+1800, IRAS 06096+1757 and IRAS 06105+1756) and two massive stars (HD 253327 and HD 253247) in the G192.584-0.041 HII region/molecular cloud complex. Both the IRAS sources and massive stars are associated with the radio continuum (NVSS).

The core contours of Fig. 5 show a dense core elongated NS surrounded by the shell structure. The core structure in CO $J = 2 - 1$ is consistent with the column density contours of ¹³CO $J = 1 - 0$ (Heyer et al. 1989) and the molecular core of CS $J = 5 - 4$ (Shirley et al. 2003). The blue and red lobes of the outflow have a similar morphology to the shell and dense core of molecular cloud, respectively.

From the outflow diagram of Fig. 5, along with Fig. 5 of Heyer et al. (1989) and Fig. 16 of Zinchenko et al. (1994), the extension of outflow of CO $J = 2 - 1$ is larger than that of CS $J = 2 - 1$, but smaller than that of CO $J = 1 - 0$. The result suggests that the outflows may be caused by stellar wind sweeping up the surrounding materials in different intensity layer. The materials of the outflows come from the surrounding materials entrained by the winds or jets from the central stars, and not from the materials ejected from the central stars.

From Fig. 5, the MSX source is centered at IRAS 06099+1800. H₂O masers 1, 2, 3 (Henkel et al. 1986; Cernotto et al. 1990; Henning et al. 1992) and class II CH₃OH maser 4 (Caswell et al. 2000) are associated with IRAS 06099+1800 and located near the maximum $R_{I_{\text{CO}(3-2)}/I_{\text{CO}(2-1)}}$ region. Class II CH₃OH masers associated with UCHII regions trace the earliest stage of massive stars and are excited by infrared radiation (Cragg, Sobolev & Godfrey 2002). H₂O masers 5 and 6 (Henning et al. 1992; Palagi et al. 1993) are located at the edge of molecular cloud.

3.1.6. S288

S288 is excited by a B0-type star ced92 and is associated with IRAS 07061-0414. The NVSS continuum peaks at IRAS 07061-0414.

In Fig. 6, the molecular cloud core extends in NE-SW direction and the peak intensity of molecular cloud core centers at IRAS 07061-0414. Another B8-type star HD 296489 lies NE of the molecular cloud core.

The outflow contours have a similar morphology to that of molecular cloud core. The MSX source is associated with the region with maximum $R_{I_{\text{CO}(3-2)}/I_{\text{CO}(2-1)}}$ of the red wing.

3.1.7. G70.293+1.600

According to the continuum observations at 2 cm and 3.6 cm (Kurtz, Churchwell & Wood 1994), the UCHII region G70.293+1.600 consists of a compact core extended EW and an elongated shell in NS. The NVSS continuum is associated with IRAS 19598+3324. IRAS 19598+3324 is at the same position as the MSX source.

From Fig. 7, the molecular cloud core and the blue lobe of the outflow in CO $J = 2 - 1$ line have a similar morphology to that of the compact core at 2 cm and 3.6 cm, and the morphology of red lobe is similar to the shell at 2 cm and 3.6 cm continuum (Kurtz, Churchwell & Wood 1994). The extension of red lobe exceeds the edge of molecular core. It is possible that the fast winds or jets entrain the surrounding materials breaking through the edge of molecular cloud and stretching out the red-shifted CO gas.

From Fig. 7, the maximum line intensity ratios of $R_{I_{\text{CO}(3-2)}/I_{\text{CO}(2-1)}}$ determined from the wings are elongated EW. H₂O masers 1, 3 and OH maser 2 (Benson et al. 1990; Argon, Reid & Menten 2000) are located along the NE-SW direction of the outflow and within the maximum $R_{I_{\text{CO}(3-2)}/I_{\text{CO}(2-1)}}$ region determined from the core component. OH masers are formed in the envelope of massive stars and indicators of newly formed O- and early B-type stars (Argon, Reid & Menten 2000). The association of the OH maser with IRAS 19598+3324 suggests that IRAS 19598+3324 is a deeply embedded young massive star. The MSX source is associated with the maximum line intensity ratio determined from the core and wings.

3.1.8. S127

S127 is associated with IRAS 21270+5423. The NVSS continuum peaks near IRAS 21270+5423. Two MSX sources are located NE and SW of IRAS 21270+5423, respectively.

Molecular cloud core has an extended structure from NE to SW (see Fig. 8). The maximum $R_{I_{\text{CO}(3-2)}/I_{\text{CO}(2-1)}}$ correlates well with the MSX source.

From the outflow diagram of Fig. 8, the two lobes of the outflow extended in the different direction. The maximum $R_{I_{\text{CO}(3-2)}/I_{\text{CO}(2-1)}}$ from the blue and red wings are related to the MSX sources in SW and NE, respectively.

3.1.9. S138

S138 is associated with IRAS 22308+5812. The O7.5-type star GRS105.63-00.34 is located east of IRAS 22308+5812. The NVSS continuum peaks at IRAS 22308+5812. The contours of CO $J = 1 - 0$ and ¹³CO $J = 1 - 0$ show a structure elongated NS and the core of C¹⁸O $J = 1 - 0$ is elongated EW (Johansson et al. 1994).

From the core diagram of Fig. 9, molecular cloud cores in CO $J = 2 - 1$ and ¹³CO $J = 2 - 1$ lines show a triangle structure. Massive stars are located at the center of the molecular cloud. Comparing with the contours of CO $J = 1 - 0$ and ¹³CO $J = 1 - 0$ (Johansson et al. 1994), the relatively warm gas of CO $J = 2 - 1$ appears to be surrounded by the cold CO $J = 1 - 0$ and ¹³CO $J = 1 - 0$ gas. The line intensity ratio determined from the core extends from the center to west. The line intensity ratio map has a similar morphology to that of the H_α image (Deharveng et al. 1999). A possible explanation is that the expanding HII region injects the hot ionized gas into the molecular core and heats the dust and molecular gas in the molecular core.

From the outflow diagram of Fig. 9, the red lobe has a similar morphology to that of the core contours of CO $J = 1 - 0$ and ¹³CO $J = 1 - 0$ (Johansson et al. 1994), and the blue lobe has a similar extension to that of the core contours of C¹⁸O $J = 1 - 0$ (Johansson et al. 1994). The extension of the red lobe exceeds the boundary of molecular core. The strong stellar winds or jets from central stars appear to be responsible for driving the red lobe of the outflow out from the core region. The MSX emission and IRAS source or massive stars are not associated with the maximum line intensity ratio of the red lobe in the outflow. It is possible that the shock is responsible for the molecular gas heating of the red lobe. The H₂O maser (Cesaroni, Palagi & Felli 1988) is overlaid at the IRAS 22308+5812 position and is located east of the maximum $R_{I_{\text{CO}(3-2)}/I_{\text{CO}(2-1)}}$ region.

3.1.10. S149

There are three IRAS sources, IRAS 22542+5815, IRAS 22546+5814 and IRAS 22543+5821 in the S149 HII region/molecular cloud complex. IRAS 22542+5815 is located near the peak of the NVSS continuum.

From Fig. 10, there are two molecular cloud cores in the S149 HII region/molecular cloud complex. The northern one is associated with IRAS 22543+5821 and the southern one is associated with IRAS 22542+5815 and IRAS 22546+5814.

The complex structure of red and blue lobes indicates multi-outflows produced in this molecular/HII region complex.

3.2. Relationship among NVSS continuum, MSX sources and line intensity ratios

In addition to the ten sources with detections of outflows discussed above, there are five sources with no detections of outflows (see Figs. 11 and 12 in Appendix A). According to Figs. 1-12, all the fifteen sources have NVSS continuum emission. The NVSS continuum peaks near or at the IRAS sources with largest far-infrared luminosities (see also Table 4) in each of the HII region/molecular cloud complexes. Except for S193, the MSX point-like sources are located near the IRAS sources with NVSS continuum. We consider an MSX source to be associated with the maximum ratios if the MSX sources are located within the range of 65'', half of the CO $J=2-1$ beam, from the peak of the ratio. Those MSX point-like sources associated with the maximum line intensity ratios of the blue and red wings and/or the core components (R_b , R_r and R_c) are presented in Table 4.

From Table 4, there are twenty-seven IRAS sources and twelve massive stars without IRAS counterparts in the fifteen regions. Of the twenty-seven IRAS sources, the twenty IRAS sources are located at or near the MSX point-like sources. In the S217 region, IRAS 04547+4753 is located at the center of the MSX 8.3 μm image although it has no MSX point-like source counterpart. Of the twelve massive stars without IRAS counterparts, only ALS6206 in the S175 region and ALS8745 in the S138 region are associated with MSX point-like source counterparts.

From Figs. 1-12, there are nineteen maximum line intensity ratio $R_{\text{I}_{\text{CO}(3-2)}/\text{I}_{\text{CO}(2-1)}}$ regions determined from core components in the fifteen HII region/molecular cloud complexes. Sixteen of the nineteen maximum line intensity ratio regions are associated with MSX point-like sources. The result shows that all the maximum line intensity ratio regions determined from core components are related to the MSX 8.3 μm emission.

Among the ten sources associated with outflows, we found that nine sources with a maximum line intensity ratio determined from blue wing appears to be related to the eleven MSX point-like sources while seven sources with a maximum line intensity ratio determined from red wings are related to the eight MSX point-like sources. However, for G213.880-11.837 and S138, we have found that there is no evidence for the maximum line intensity ratios of the red-shifted wings in these sources associated with either MSX sources or IRAS sources or massive stars.

Based on our sample discussed in this paper, there are 78% IRAS sources are found to be associated with MSX 8.3 μm emission. For the core components, 87% of the maximum line intensity ratio regions appears to be associated with MSX sources. For both the blue and red wings, about 90% and 70% of maximum line intensity ratio regions are associated with MSX sources. Our analysis suggests that there is a possible relationship between the regions with maximum line intensity ratios and the MSX 8.3 μm as well as FIR emission.

4. Discussion

4.1. Outflows

Ten molecular outflows were identified out of the fifteen HII region/molecular cloud complexes observed in this program. All outflows in our sample show poor collimation except for G213.880-11.837. However, the angular resolution (130'' in CO $J = 2 - 1$) corresponds to a linear scale range of 0.3–7.5 pc for the program sources at the distances ranging from 0.5 to 11.5 kpc. Our angular resolution appears to be not adequate to image the highly collimated outflow in a smaller scale. Thus, the outflow detection rate from our KOSMA observations only imposes a lower limit. Nevertheless, higher outflow detection rate (67%) suggests that in the process of high-mass star formation, outflows appear to be common phenomena, which is consistent with the results obtained from other groups (Beuther et al. 2002; Shepherd & Churchwell 1996b). Beuther et al. (2002) selected twenty-six massive star forming regions prior to the stage of UCHII regions and identified twenty-one massive molecular outflows. Shepherd & Churchwell (1996b) iden-

tified five massive molecular outflows from ten massive star forming regions associated with UCHII regions. All the fifteen sources in our sample have $\text{H}\alpha$ emission from the red plate of POSS survey and are in relatively evolved stages. When combined with the results of Beuther et al. (2002) and Shepherd & Churchwell (1996b), the outflows appear to present in the evolutionary stages from the high mass protostars and UCHII regions to the HII regions in the process of massive star formation.

Many models for the origin of the outflows have been discussed (e.g. Lada 1985; Shu et al. 1991). The molecular outflows were commonly thought to be driven by winds or jets from the energy sources located in the molecular clouds. The winds and jets likely sweep up the ambient materials around central stars and create the outflow structure (Lada 1985; Shu et al. 1991). In the high mass star forming regions, the outflow likely plays the same important role in dissipating energy and angular momentum as those in low-mass star formation regions.

Comparing the extension of the outflows with that of molecular cores, the scale of the outflows except for S138 and G70.293+1.600 appears not to exceed the edge of molecular cloud cores. The peaks of the integrated intensity in the red and blue lobes of the outflows in our sample are close to the peaks of their associated molecular cores. A possible driving mechanism of the outflows is that the surrounding materials are entrained by the winds or jets as the winds or jets pass through the inhomogeneous molecular clouds. As a result, the larger integrated intensities of red and blue lobes in the outflows are close to the dense regions in the molecular cloud cores. Comparing the far-infrared luminosities with the masses of the outflows in Table 3, the sources with higher far-infrared luminosities appear to have larger outflow masses. This is consistent with the result found by Shepherd & Churchwell (1996b). From Table 3, the outflow masses (except for G213.880-11.837 and S288 with 11 and 33 M_{\odot}) in our sample are greater than 83 M_{\odot} , which is far greater than the mass of O4-type star. The larger outflows mass suggests that the outflow masses are not likely to originate from the stellar surface, but could be caused by the entrainment of ambient gas (Shepherd & Churchwell 1996b).

4.2. Heating mechanism

The molecular clouds associated with HII regions have higher line intensity ratio of CO $J = 3 - 2$ to CO $J = 2 - 1$ lines and have higher temperature than those sources without HII regions (Wilson, Walker & Thornley 1997). The association of the higher line intensity ratios with the IRAS sources implies that the molecular gas could be heated by the thermal emission of dust (Goldreich & Kwan 1974). Cohen & Green (2001) carried out a survey at 8.3 μm and 834 MHz toward thermal and non-thermal radio sources covering area of $310^{\circ}.4 \leq l \leq 313^{\circ}.7$ and $-0^{\circ}.9 \leq b \leq 1^{\circ}.4$. There is a complete absence in this field of any detected MSX 8.3 μm counterparts to non-thermal radio sources. The result suggests that MSX 8.3 μm emission is dominated by the thermal emission of dust and the dust is heated by the radiation from massive stars (Cohen & Green 2001).

We found that about 87% of maximum line intensity ratio regions from core components in our sample are associated with MSX point-like sources. All the IRAS sources with NVSS continuum (except for S193 region) have MSX 8.3 μm emission. A possible explanation is that massive stars with IRAS counterparts are still deeply embedded in their parental gas/dust envelope. The dust acts as a kind of buffer which absorbs the UV radiation leaking from the HII region associated with massive stars and reradiates at the far-infrared and mid-infrared bands so that the molecules in the core would not be destroyed in the heating process. The straightforward statistics in our analysis do favor that the radiation from far-infrared and mid-infrared is the main heating source to the gas in the molecular cores.

Alternatively, for G213.880-11.837, the 12.5 μm image (Persi & Tapia 2003) has similar morphology to that of continuum at 2 cm (Gomez et al. 1998, 2000). The line intensity ratio map from the core of S138 has a similar morphology to that of the $\text{H}\alpha$ image (Deharveng et al. 1999). It is possible that the expanding HII regions inject the hot ionized gas into the molecular cores and lead to the increase in temperature of both dust and molecular gas in the two molecular cores in the G213.880-11.837 and S138 regions.

We note that for the ten sources associated with the outflows, higher rate in detection of MSX emission in maximum line intensity ratio regions associated with the blue and red wings suggested that molecular gas in the outflows appears to be mainly heated by the emission of dust. However, heating through shocks can not be excluded. For example, the maximum line intensity ratio determined from red-shifted lobes in G213.880-11.837 and S138 regions are far away from any radiative heating sources including IRAS, MSX and HII emission. Shocks produced by the interaction between the outflows and molecular clouds might be a plausible heating mechanism for the red lobe in the outflows of G213.880-11.837 and S138.

Furthermore, from the literatures, H_2O masers were only detected in seven regions in our sample (S201, G206.543-16.347, G139.909+0.197, G192.584-0.041, G213.880-11.837, G70.293+1.600 and S138). The model based on the shock structure and maser pumping scheme (Elitzur, Hollenbach & McKee 1989) suggested that in star forming regions, H_2O maser emission results from dense regions behind shock. The observations showed that most of H_2O masers were found along the axes of the outflows (e.g. Garay & Lizano 1999). The CO outflows with high mechanical luminosities were associated with H_2O masers (Felli, Palagi & Tofani 1992). The fact that H_2O masers were associated with outflows with high mechanical luminosities and observed along the axes of the outflows suggested that only winds with high mechanical luminosities can produce shocks to excite H_2O masers. The observations also showed that H_2O masers occur in relatively warm regions (e.g. Codella, Testi & Cesaroni 1997). Comparing with the images of CO lines, the masers are located within the maximum line intensity ratio regions and associated with the outflows with high mechanical luminosities and MSX 8.3 μm emission. The results are consistent with the model that H_2O masers are related to the outflows and occur in relatively warm environments (Elitzur, Hollenbach & McKee 1989; Felli,

Palagi & Tofani 1992; Codella, Testi & Cesaroni 1997; Garay & Lizano 1999).

5. Conclusions

From our observations and analysis, we found ten molecular outflows out of fifteen HII region/molecular cloud complexes in our sample. Higher outflow detection rate (67%) appears to indicate that outflow plays an important role in the formation process of high-mass stars. The HII regions in our sample are relatively evolved. When combined with the detections of outflow toward protostar cores (Beuther et al. 2002) and UCHII regions (Shepherd & Churchwell 1996b), the massive molecular outflows might occur in all stages of massive star formation.

Comparing the morphology of outflows with that of molecular cores, the outflows appear to result from the surrounding materials that are entrained by the winds or jets from central stars.

The maximum line intensity ratios determined from the molecular cores and outflows are highly associated with the MSX 8.3 μm emission. The molecular gas in the outflows and cores appears to be mainly heated by the emission of dust. In a few cases of outflows, shock heating might be inevitable.

Based on previous observations in the literatures, H_2O masers are located near the massive stars of the seven HII region/molecular cloud complexes. The correlation among H_2O masers, the outflows and the maximum line intensity ratios is consistent with the result that H_2O masers are related to the outflows and occur in relatively warm environments.

Acknowledgements. We thank anonymous referee for his/her constructive suggestions. This work is supported by the National Natural Science Foundation of China under Grant Nos. 10473014, 10328306, 10521001 and 10433010. This work is also supported by National Basic Research Program of China (973 program) under grant No. 2007CB815103 and Chinese Academy Sciences under Grant No. KJCX2-YW-T01. Sheng-Li Qin thanks Ms. Ni-Mei Chen for her help during the observations.

Appendix A: Sources Without Outflow

1. S175

The optical HII region S175 is excited by an O9.5-type star ALS 6206 (White & Gee 1986). IRAS 00244+6425 is located near the O9.5-type star ALS 6206. The NVSS continuum peaks at IRAS 00244+6425.

In the left panel of Fig. 11, the contours of CO $J = 2 - 1$ have a morphology similar to that of ^{13}CO $J = 2 - 1$. The MSX source and IRAS 00243+6427 are located within the maximum $R_{\text{CO}(3-2)}/I_{\text{CO}(2-1)}$ region.

2. S193

The molecular cloud/HII region complex S193 harbors three HII regions, S192, S193 and S194. IRAS 02437+6145 is associated with the NVSS continuum. Additional two IRAS sources of IRAS 02435+6144 and IRAS 02439+6143 are also located in this region.

The molecular cloud core has two peaks (see Fig. 11), the south one is associated with IRAS 02435+6144. The MSX

source and IRAS 02435+6144 are located within the maximum $R_{I_{\text{CO}(3-2)}/I_{\text{CO}(2-1)}}$ region.

3. S201

IRAS 02593+6016 is associated with the HII region/molecular cloud complex. The continuum at 2 and 6 cm are excited by IRAS 02593+6016, and the H₂O masers 1 and 2 (Cesaroni, Palagi & Felli 1988; Palagi, Cesaroni & Comoretto 1993) are close to the continuum peak at 1.4 GHz (NVSS), 2 and 6 cm (Felli, Hjellming & Cesaroni 1987). IRAS 02593+6016 is overlaid at the MSX source position.

From S201 diagram of Fig. 12, the molecular cloud extends in the EW direction. The maximum $R_{I_{\text{CO}(3-2)}/I_{\text{CO}(2-1)}}$ is far away from the IRAS 02589+6014.

4. S217

There are two massive stars, O9.5-type star LSV 47°24 and B8-type star BD+47 1079 and two IRAS sources, IRAS 04551+4755 and IRAS 04547+4753 located within the S217 HII region /molecular cloud complex.

From the right diagram of Fig. 12, the molecular cloud core associated with S217 has an elongated structure. The strongest emission is located to the SW of molecular cloud, and centered at IRAS 04547+4753. The intensity falls off gradually from SW to NE. Comparing with the NVSS continuum and Fig. 1 of Roger & Leahy (1993), the peak of the 21 cm continuum is located at the same position as CO peak; the O9.5-type star LSV 47°24 (Roger & Leahy 1993) is located NE about 3' of IRAS 04547+4753; the B8-type star BD+47 1079 is close to the northern weaker molecular core.

The line intensity ratio map shows that the maximum value of $R_{I_{\text{CO}(3-2)}/I_{\text{CO}(2-1)}}$ is close to IRAS 04547+4753. The extended MSX 8.3 μm emission is centered at IRAS 04547+4753 but there is no MSX point source in this region.

5. G206.543-16.347

G206.543-16.347 is associated with IRAS 05393-0156. Molecular cloud core in ¹³CO $J = 2-1$ contours shows an elongated structure in NS, but the core contours in CO $J = 2-1$ shows an amorphous structure. H₂O maser (Palagi, Cesaroni & Comoretto 1993) is located south of IRAS 05393-0156 and within maximum $R_{I_{\text{CO}(3-2)}/I_{\text{CO}(2-1)}}$ region. The brightest emission at MSX 8.3 μm is consistent with the maximum $R_{I_{\text{CO}(3-2)}/I_{\text{CO}(2-1)}}$ region.

We fail to detect a highly collimated outflow that had been observed in CO $J = 2-1$ with an angular resolution of 23'' by Sanders & Willner (1985), which may be caused by low resolution from our observations.

Appendix B: Figures

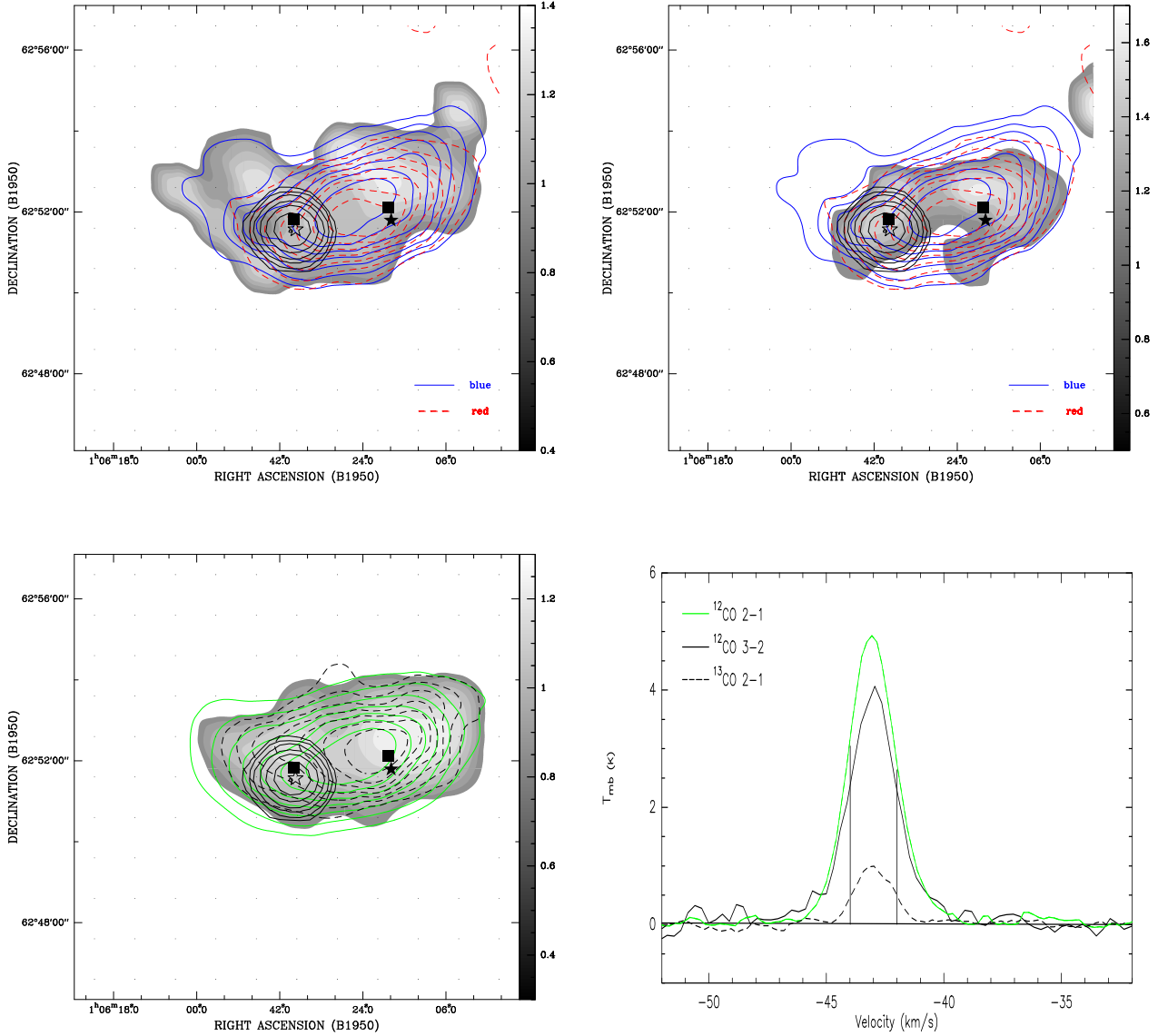


Fig. B.1. S186. Top-left panel: outflow contours (blue and red-shifted components are shown as blue solid and red dashed lines) are superimposed on the line intensity ratio map (grey scale) of the blue wing. Top-right panel: outflow contours are superimposed on the intensity ratio map (grey scale) of the red wing. Bottom-left panel: the integrated intensity map of the core in CO $J = 2 - 1$ (green solid contours) are superimposed on the grey map of the line intensity ratio from the core component, and the dashed contours are the integrated intensity map of the core in $^{13}\text{CO } J = 2 - 1$ line. The thin solid lines show the continuum at 1.4 GHz from NVSS. The contours for the cores begin at 30% of the maximum integrated intensity I_{max} and increase at a step of 10% of I_{max} , and the integrated line intensity ratios range from 30% of the maximum $R_{I_{\text{CO}(3-2)}/I_{\text{CO}(2-1)}}$ to the maximum $R_{I_{\text{CO}(3-2)}/I_{\text{CO}(2-1)}}$. The intensity ratios indicate the gas temperature variations at different positions. The unfilled and filled stars mark IRAS 01056+6251 and IRAS 01053+6251, respectively. The filled square symbols indicate the MSX source. The dot symbols mark the mapped points. Bottom-right panel: the spectra averaged over the outflow zones (the CO $J = 3 - 2$ data were smoothed to the resolution of the $J = 2 - 1$ observations); the vertical lines indicate the beginning of the blue and red wings.

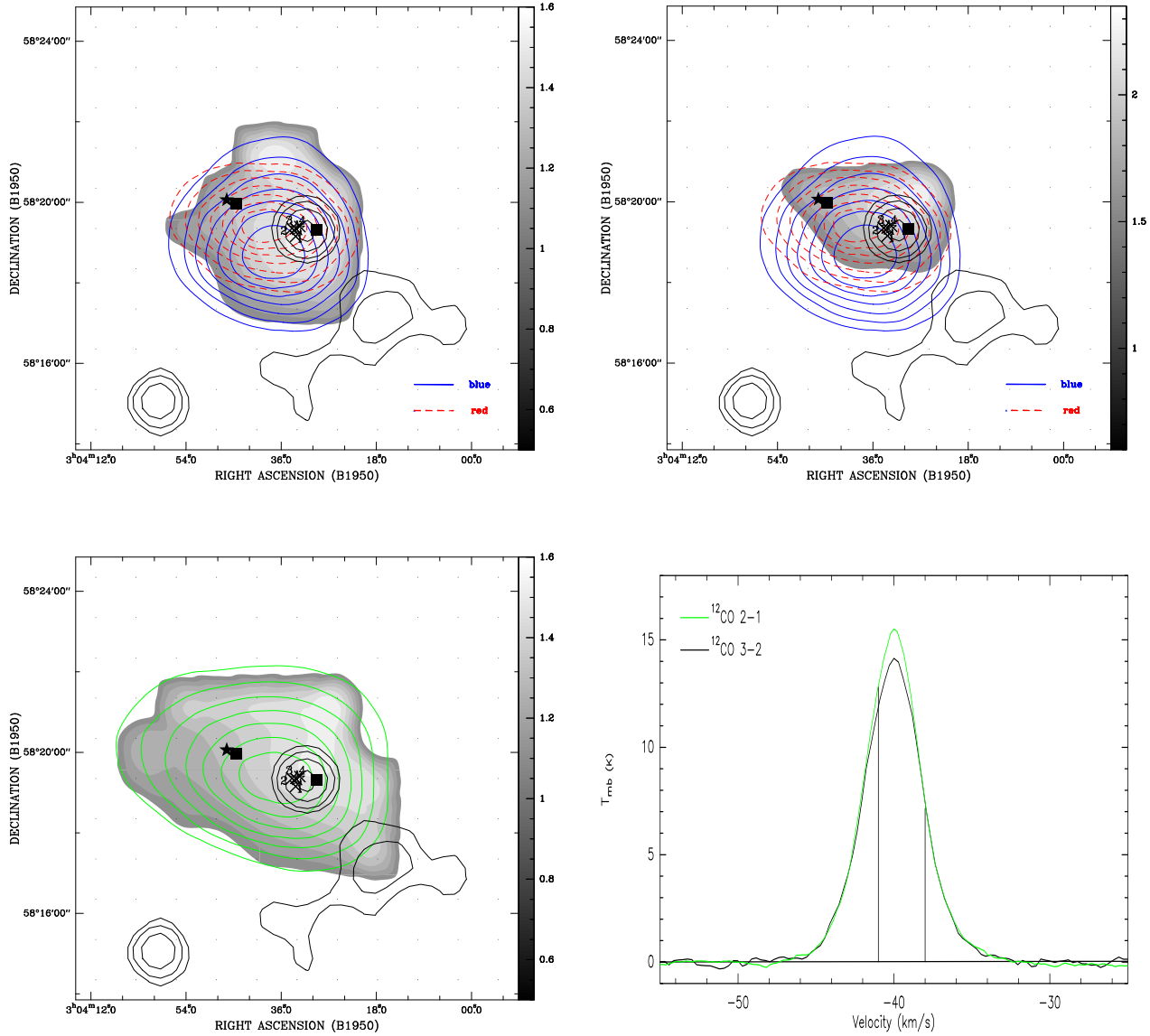


Fig. B.2. G139.909+0.197. Top-left panel: outflow contours (blue and red-shifted components are shown as blue solid and red dashed lines) are superimposed on the line intensity ratio map (grey scale) of the blue wing. Top-right panel: outflow contours are superimposed on the line intensity ratio map (grey scale) of the red wing. Bottom-left panel: the integrated intensity map of the core in CO $J = 2 - 1$ (green solid contours) are superimposed on the grey map of the line intensity ratio from the core component. The thin solid lines show the continuum at 1.4 GHz from NVSS. The contours for the cores begin at 30% of the maximum integrated intensity I_{\max} and increase at a step of 10% of I_{\max} , and the integrated line intensity ratios range from 30% of the maximum $R_{I_{\text{CO}(3-2)}/I_{\text{CO}(2-1)}}$ to the maximum $R_{I_{\text{CO}(3-2)}/I_{\text{CO}(2-1)}}$. The intensity ratios indicate the gas temperature variations at different positions. The filled star is IRAS 03037+5819, and unfilled star marks IRAS 03035+5819. The cross symbol 1 is SiO maser, and the rest crosses 2, 3 and 4 indicate H₂O masers. Bottom-right panel: the spectra averaged over the outflow zones (the CO $J = 3 - 2$ data were smoothed to the resolution of the $J = 2 - 1$ observations); the vertical lines indicate the beginning of the blue and red wings.

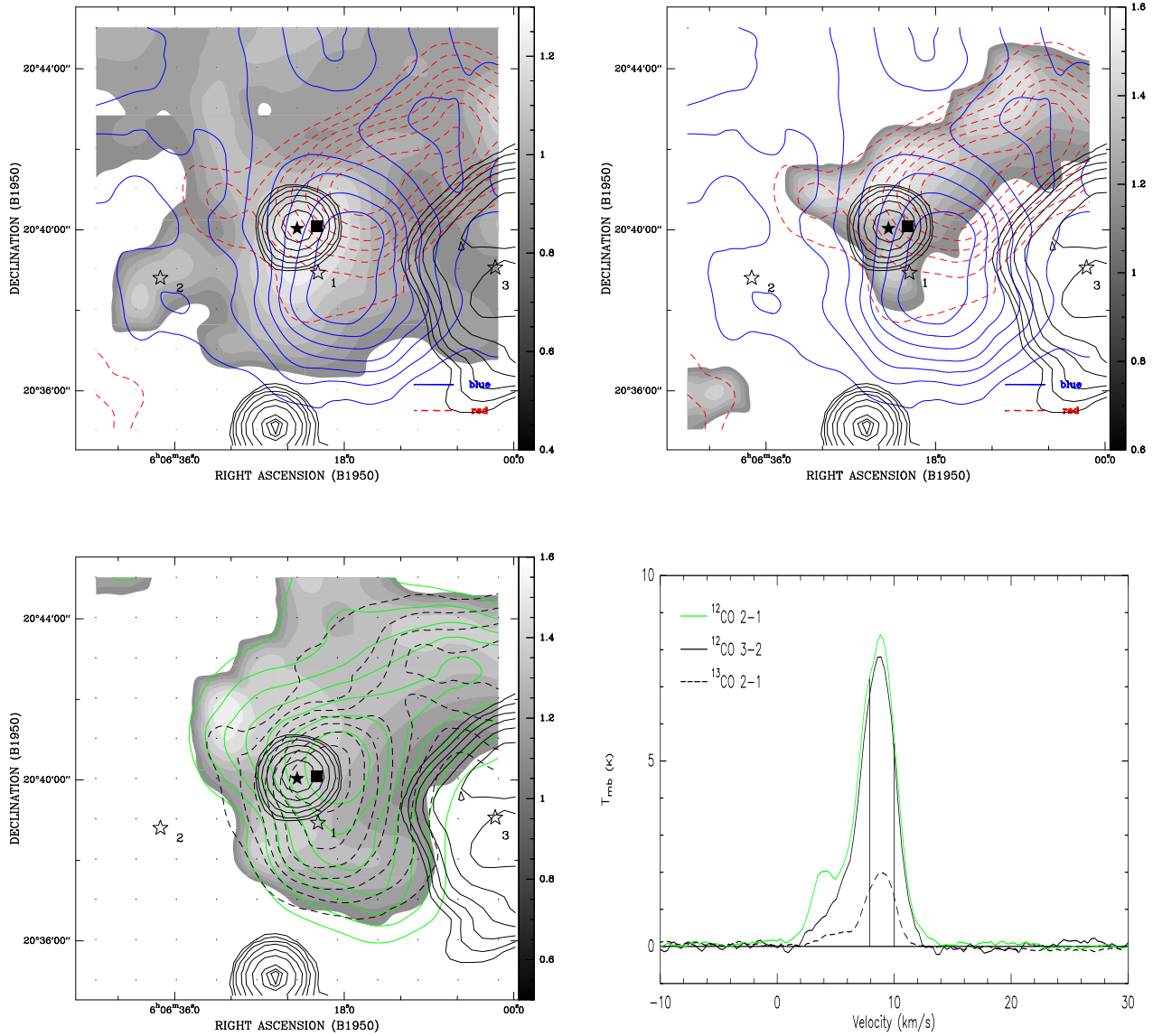


Fig. B.3. G189.876+0.516. Top-left panel: outflow contours (blue and red-shifted components are shown as blue solid and red dashed lines) are superimposed on the line intensity ratio map (grey scale) of the blue wing. Top-right panel: outflow contours are superimposed on the line intensity ratio map (grey scale) of the red wing. Bottom-left panel: the integrated intensity map of the core in CO $J = 2 - 1$ (green solid contours) are superimposed on the grey map of the line intensity ratio from the core component, and the dashed contours are the integrated intensity map of the core in $^{13}\text{CO } J = 2 - 1$ line. The thin solid lines show the continuum at 1.4 GHz from NVSS. The contours for the cores begin at 30% of the maximum integrated intensity I_{max} and increase at a step of 10% of I_{max} , and the integrated line intensity ratios range from 30% of the maximum $R_{I_{\text{CO}(3-2)}/I_{\text{CO}(2-1)}}$ to the maximum $R_{I_{\text{CO}(3-2)}/I_{\text{CO}(2-1)}}$. The intensity ratios indicate the gas temperature variations at different positions. The unfilled stars 1, 2, 3 are B-type stars ALS 8745, ALS 8748 and B1-type star HD 252325, respectively; the filled star marks IRAS 06063+2040. Bottom-right panel: the spectra averaged over the outflow zones (the CO $J = 3 - 2$ data were smoothed to the resolution of the $J = 2 - 1$ observations); the vertical lines indicate the beginning of the blue and red wings.

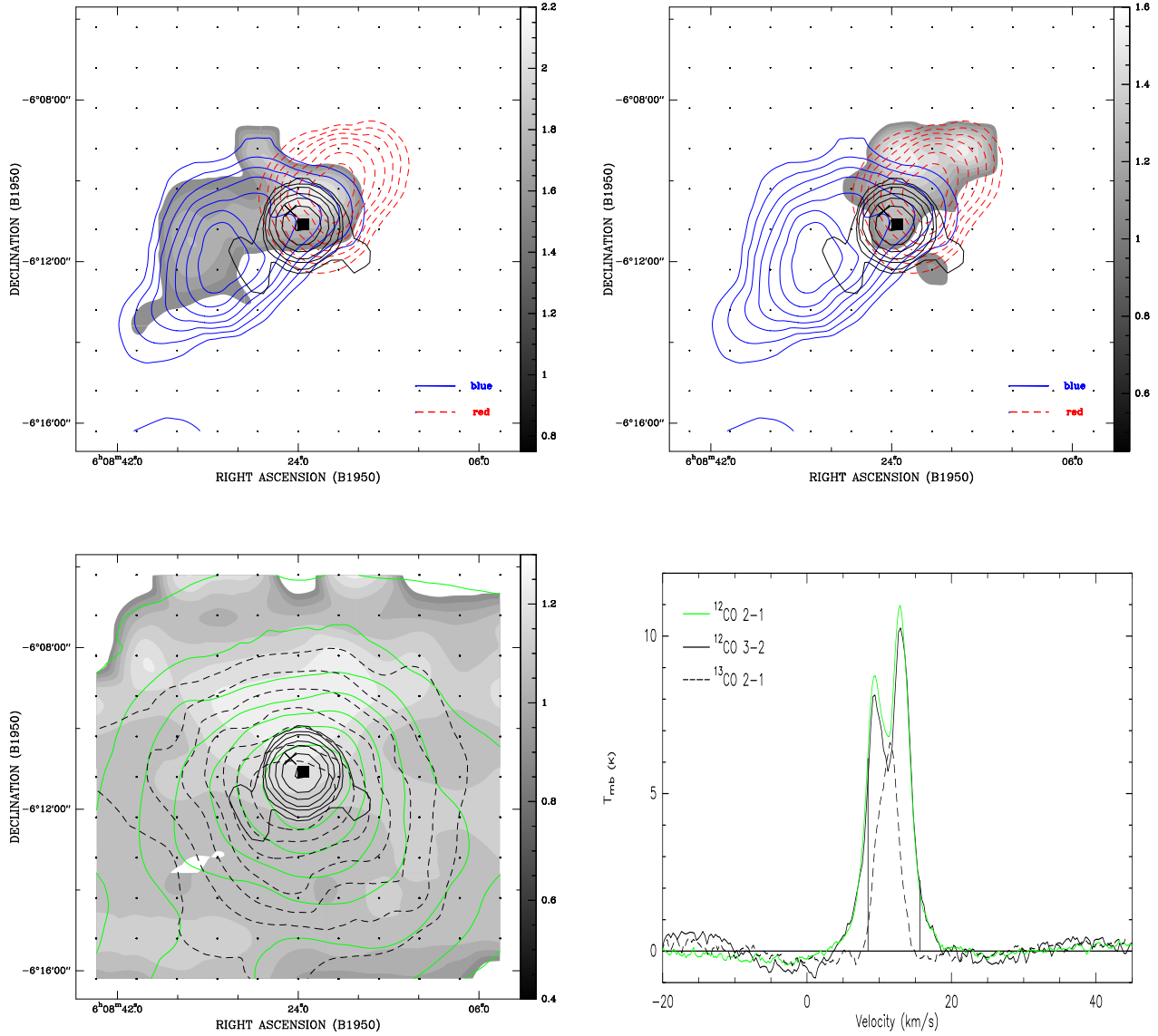


Fig. B.4. G213.880-11.837. Top-left panel: outflow contours (blue and red-shifted components are shown as blue solid and red dashed lines) are superimposed on the line intensity ratio map (grey scale) of the blue wing. Top-right panel: outflow contours are superimposed on the line intensity ratio map (grey scale) of the red wing. Bottom-left panel: the integrated intensity map of the core in CO $J = 2 - 1$ (green solid contours) are superimposed on the grey map of the line intensity ratio from the core component, and the dashed contours are the integrated intensity map of the core in $^{13}\text{CO } J = 2 - 1$ line. The thin solid lines show the continuum at 1.4 GHz from NVSS. The contours for the cores begin at 30% of the maximum integrated intensity I_{max} , and increase at a step of 10% of I_{max} , and the integrated line intensity ratios range from 30% of the maximum $R_{\text{CO}(3-2)/\text{CO}(2-1)}$ to the maximum $R_{\text{CO}(3-2)/\text{CO}(2-1)}$. The intensity ratios indicate the gas temperature variations at different positions. The filled square symbol marks the peak of $8.7 \mu\text{m}$ emission. IRAS 06084-0611 is located at the same position as the $8.7 \mu\text{m}$ emission. The cross symbol marks H_2O maser. Bottom-right panel: the spectra averaged over the outflow zones (the CO $J = 3 - 2$ data were smoothed to the resolution of the $J = 2 - 1$ observations); the vertical lines indicate the beginning of the blue and red wings.

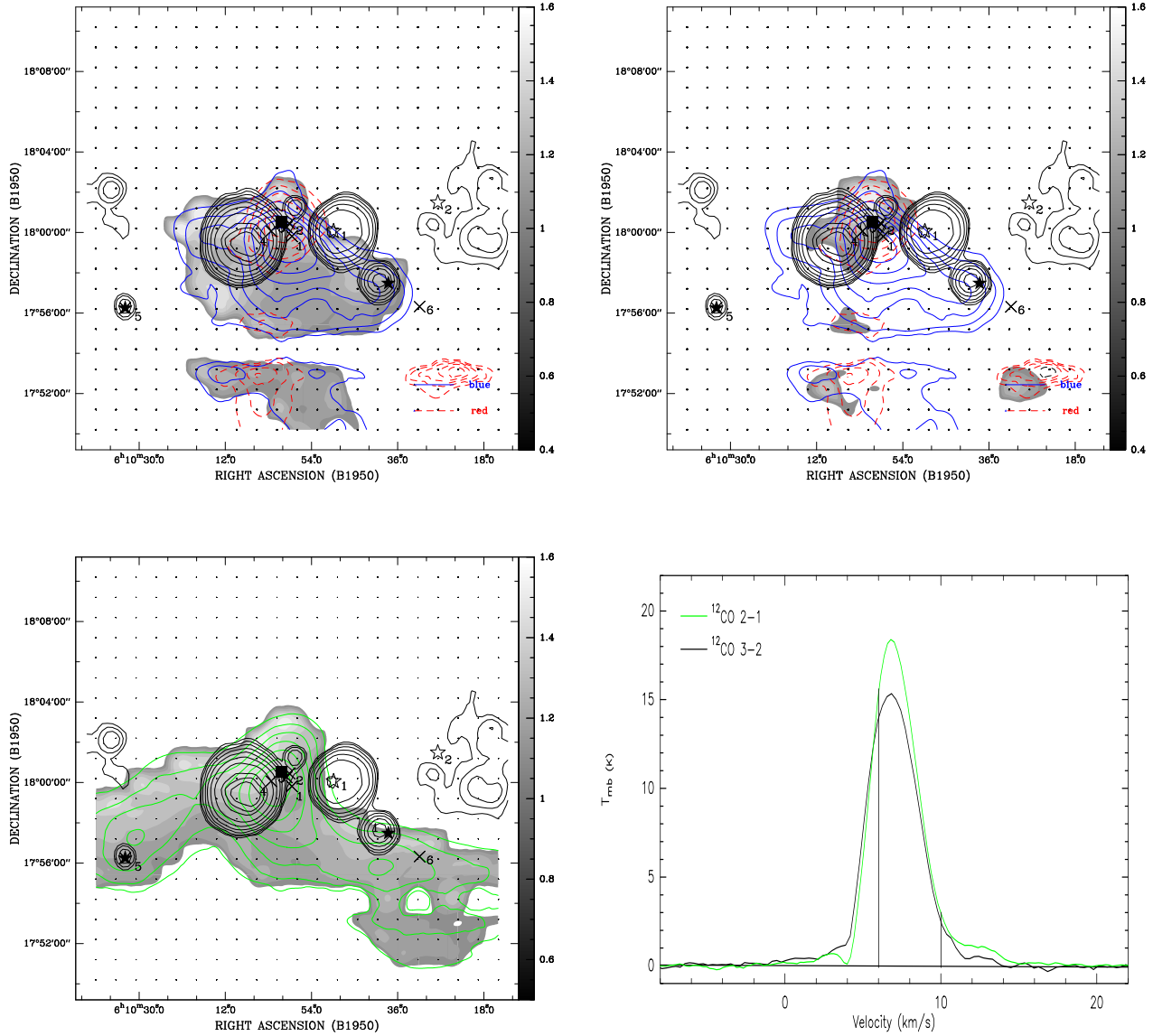


Fig. B.5. G192.584-0.041. Top-left panel: outflow contours (blue and red-shifted components are shown as blue solid and red dashed lines) are superimposed on the line intensity ratio map (grey scale) of the blue wing. Top-right panel: outflow contours are superimposed on the line intensity ratio map (grey scale) of the red wing. Bottom-left panel: the integrated intensity map of the core in CO $J = 2 - 1$ (green solid contours) are superimposed on the grey map of the line intensity ratio from the core component. The thin solid lines show the continuum at 1.4 GHz from NVSS. The contours for the cores begin at 30% of the maximum integrated intensity I_{\max} and increase at a step of 10% of I_{\max} , and the integrated line intensity ratios range from 30% of the maximum $R_{I_{\text{CO}(3-2)}/I_{\text{CO}(2-1)}}$ to the maximum $R_{I_{\text{CO}(3-2)}/I_{\text{CO}(2-1)}}$. The intensity ratios indicate the gas temperature variations at different positions. The unfilled stars 1 and 2 are B0.5-type star HD 253327 and B1-star HD 253247; the filled stars are IRAS 06105+1756 and IRAS 06096+1757. The cross symbols 1, 2, 3, 5 and 6 indicate H_2O masers, the cross symbol 4 is class II CH_3OH maser. The filled square symbol marks the MSX source. IRAS 06099+1800 is located at the MSX source position. Bottom-right panel: the spectra averaged over the outflow zones (the CO $J = 3 - 2$ data were smoothed to the resolution of the $J = 2 - 1$ observations); the vertical lines indicate the beginning of the blue and red wings.

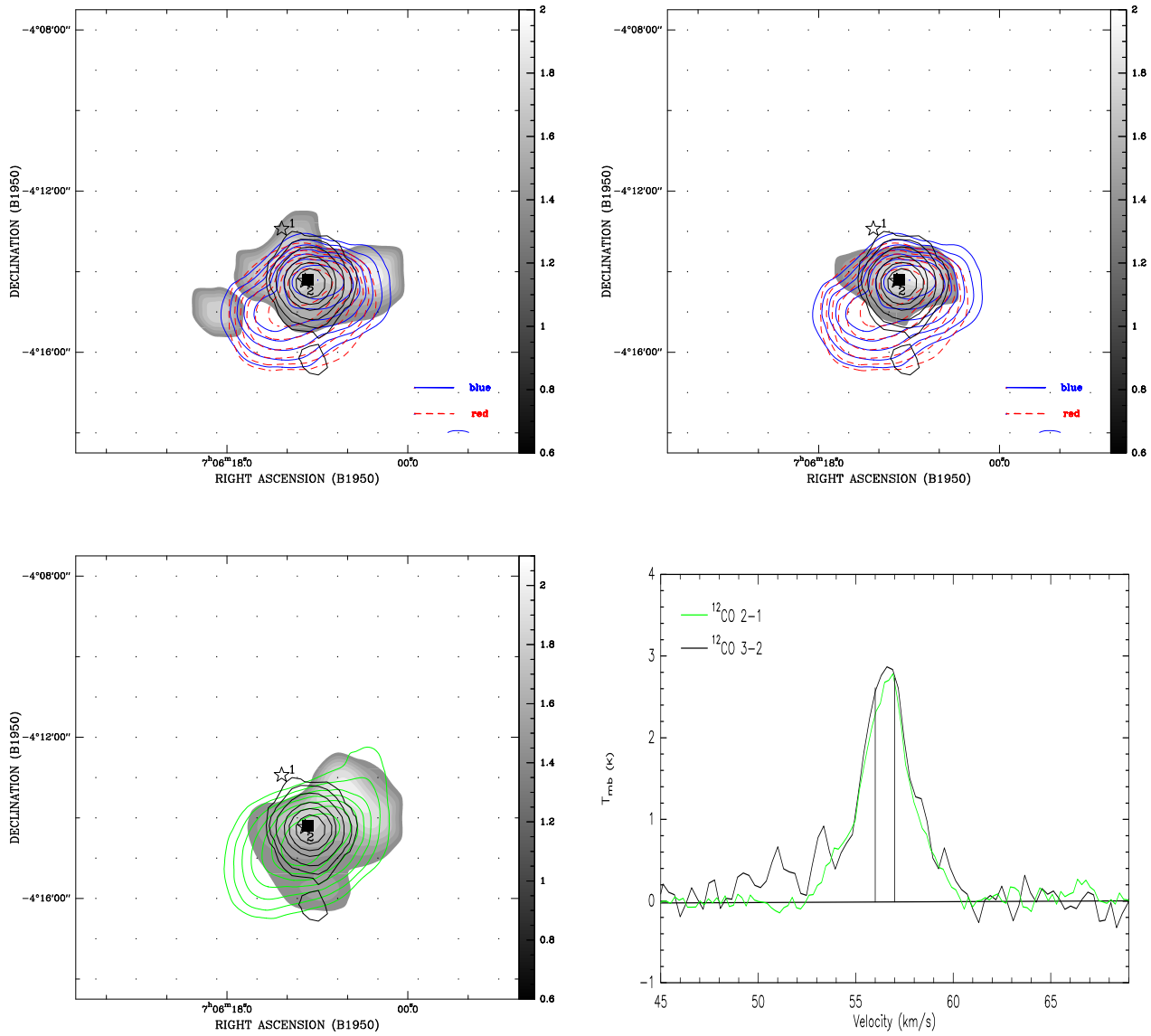


Fig. B.6. S288. Top-left panel: outflow contours (blue and red-shifted components are shown as blue solid and red dashed lines) are superimposed on the line intensity ratio map (grey scale) of the blue wing. Top-right panel: outflow contours are superimposed on the line intensity ratio map (grey scale) of the red wing. Bottom-left panel: the integrated intensity map of the core in CO $J = 2 - 1$ (green solid contours) are superimposed on the grey map of the line intensity ratio from the core component. The thin solid lines show the continuum at 1.4 GHz from NVSS. The contours for the cores begin at 30% of the maximum integrated intensity I_{max} and increase at a step of 10% of I_{max} , and the integrated line intensity ratios range from 30% of the maximum $R_{\text{CO}(3-2)/\text{CO}(2-1)}$ to the maximum $R_{\text{CO}(3-2)/\text{CO}(2-1)}$. The intensity ratios indicate the gas temperature variations at different positions. The star 1 is B8-type star HD 296489. The star 2 is B0-type star Ced 92 associated with IRAS 07061-0414. Bottom-right panel: the spectra averaged over the outflow zones (the CO $J = 3 - 2$ data were smoothed to the resolution of the $J = 2 - 1$ observations); the vertical lines indicate the beginning of the blue and red wings.

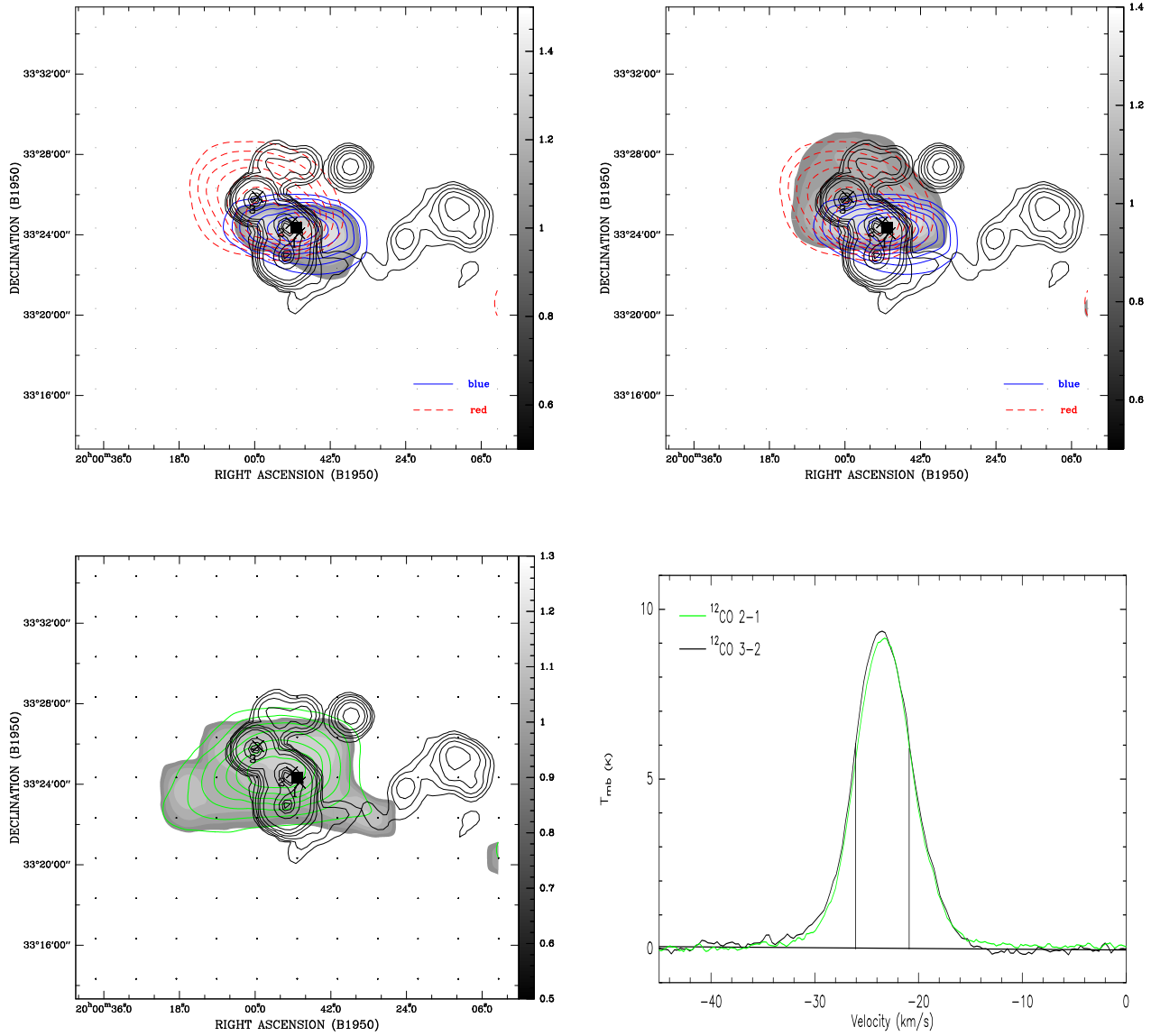


Fig. B.7. G70.293+1.600. Top-left panel: outflow contours (blue and red-shifted components are shown as blue solid and red dashed lines) are superimposed on the line intensity ratio map (grey scale) of the blue wing. Top-right panel: outflow contours are superimposed on the line intensity ratio map (grey scale) of the red wing. Bottom-left panel: the integrated intensity map of the core in CO $J = 2 - 1$ (green solid contours) are superimposed on the grey map of the line intensity ratio from the core component. The thin solid lines show the continuum at 1.4 GHz from NVSS. The contours for the cores begin at 30% of the maximum integrated intensity I_{\max} and increase at a step of 10% of I_{\max} , and the integrated line intensity ratios range from 30% of the maximum $R_{I_{\text{CO}(3-2)}/I_{\text{CO}(2-1)}}$ to the maximum $R_{I_{\text{CO}(3-2)}/I_{\text{CO}(2-1)}}$. The intensity ratios indicate the gas temperature variations at different positions. The cross symbols 1, 3 mark H_2O masers and 2 is OH maser. Bottom-right panel: the spectra averaged over the outflow zones (the CO $J = 3 - 2$ data were smoothed to the resolution of the $J = 2 - 1$ observations); the vertical lines indicate the beginning of the blue and red wings.

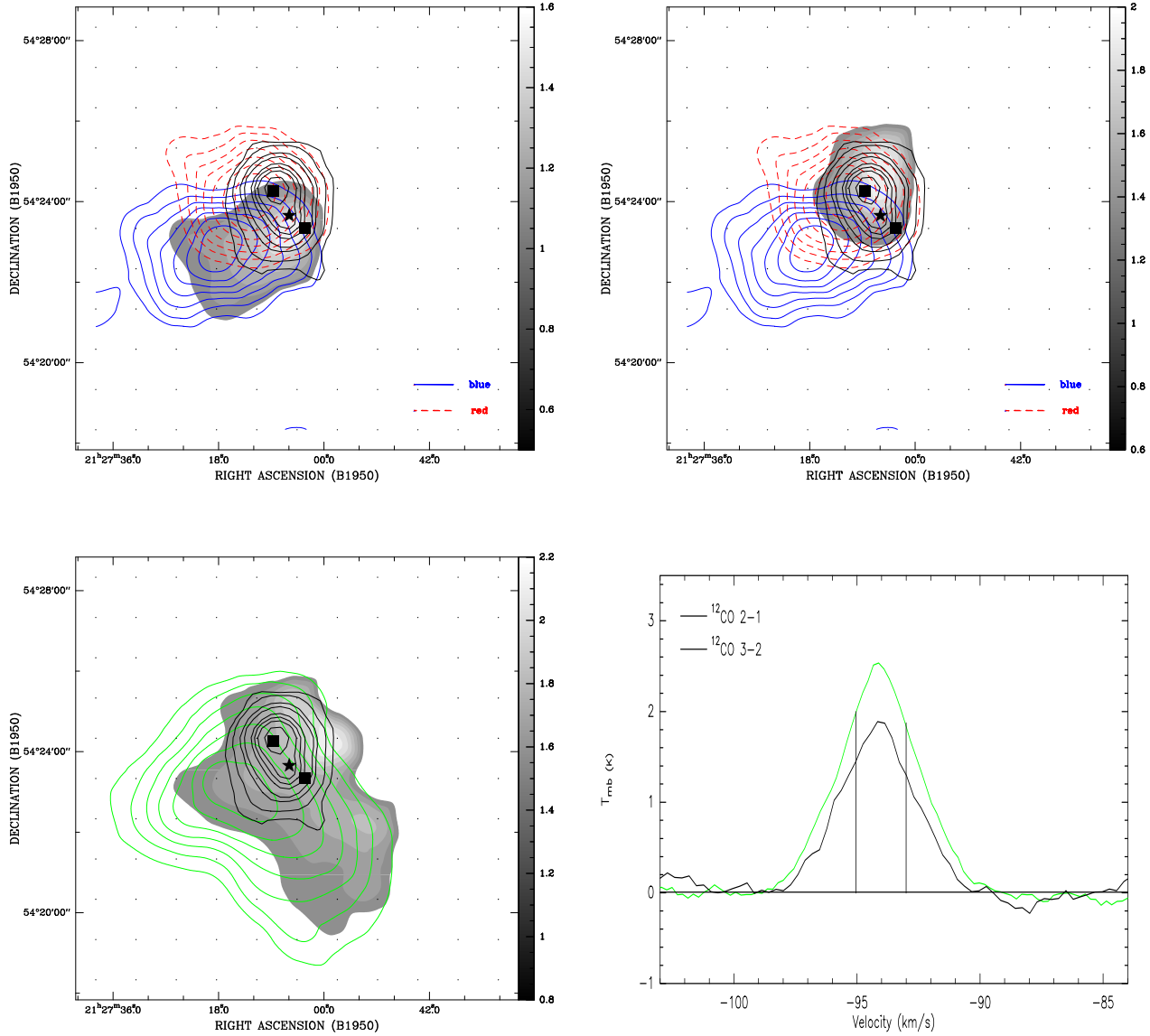


Fig. B.8. S127. Top-left panel: outflow contours (blue and red-shifted components are shown as blue solid and red dashed lines) are superimposed on the line intensity ratio map (grey scale) of the blue wing. Top-right panel: outflow contours are superimposed on the line intensity ratio map (grey scale) of the red wing. Bottom-left panel: the integrated intensity map of the core in CO $J = 2 - 1$ (green solid contours) are superimposed on the grey map of the line intensity ratio from the core component. The thin solid lines show the continuum at 1.4 GHz from NVSS. The contours for the cores begin at 30% of the maximum integrated intensity I_{\max} and increase at a step of 10% of I_{\max} , and the integrated line intensity ratios range from 30% of the maximum $R_{\text{CO}(3-2)/\text{CO}(2-1)}$ to the maximum $R_{\text{CO}(3-2)/\text{CO}(2-1)}$. The intensity ratios indicate the gas temperature variations at different positions. The star symbol marks IRAS 21270+5423. Bottom-right panel: the spectra averaged over the outflow zones (the CO $J = 3 - 2$ data were smoothed to the resolution of the $J = 2 - 1$ observations); the vertical lines indicate the beginning of the blue and red wings.

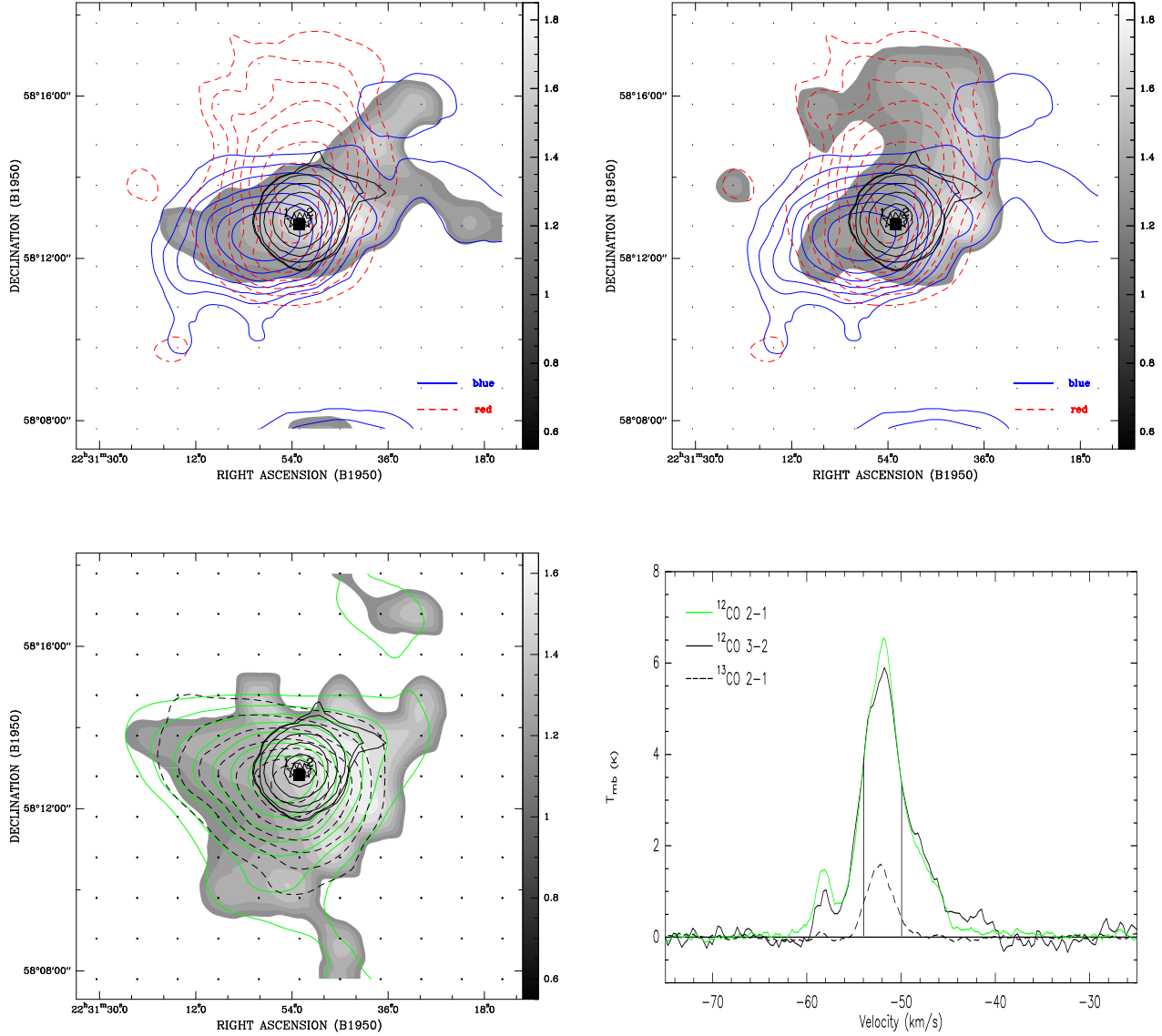


Fig. B.9. S138. Top-left panel: outflow contours (blue and red-shifted components are shown as blue solid and red dashed lines) are superimposed on the line intensity ratio map (grey scale) of the blue wing. Top-right panel: outflow contours are superimposed on the line intensity ratio map (grey scale) of the red wing. Bottom-left panel: the integrated intensity map of the core in CO $J = 2 - 1$ (green solid contours) are superimposed on the grey map of the line intensity ratio from the core component, and the dashed contours are the integrated intensity map of the core in $^{13}\text{CO } J = 2 - 1$ line. The thin solid lines show the continuum at 1.4 GHz from NVSS. The contours for the cores begin at 30% of the maximum integrated intensity I_{max} and increase at a step of 10% of I_{max} , and the integrated line intensity ratios range from 30% of the maximum $R_{I_{\text{CO}(3-2)}/I_{\text{CO}(2-1)}}$ to the maximum $R_{I_{\text{CO}(3-2)}/I_{\text{CO}(2-1)}}$. The intensity ratios indicate the gas temperature variations at different positions. The Stars 1 and 2 mark IRAS 22308+5812 and O7.5-type star GRS 105.63-00.34. H_2O maser is overlaid at the IRAS 22308+5812 position. Bottom-right panel: the spectra averaged over the outflow zones (the CO $J = 3 - 2$ data were smoothed to the resolution of the $J = 2 - 1$ observations); the vertical lines indicate the beginning of the blue and red wings.

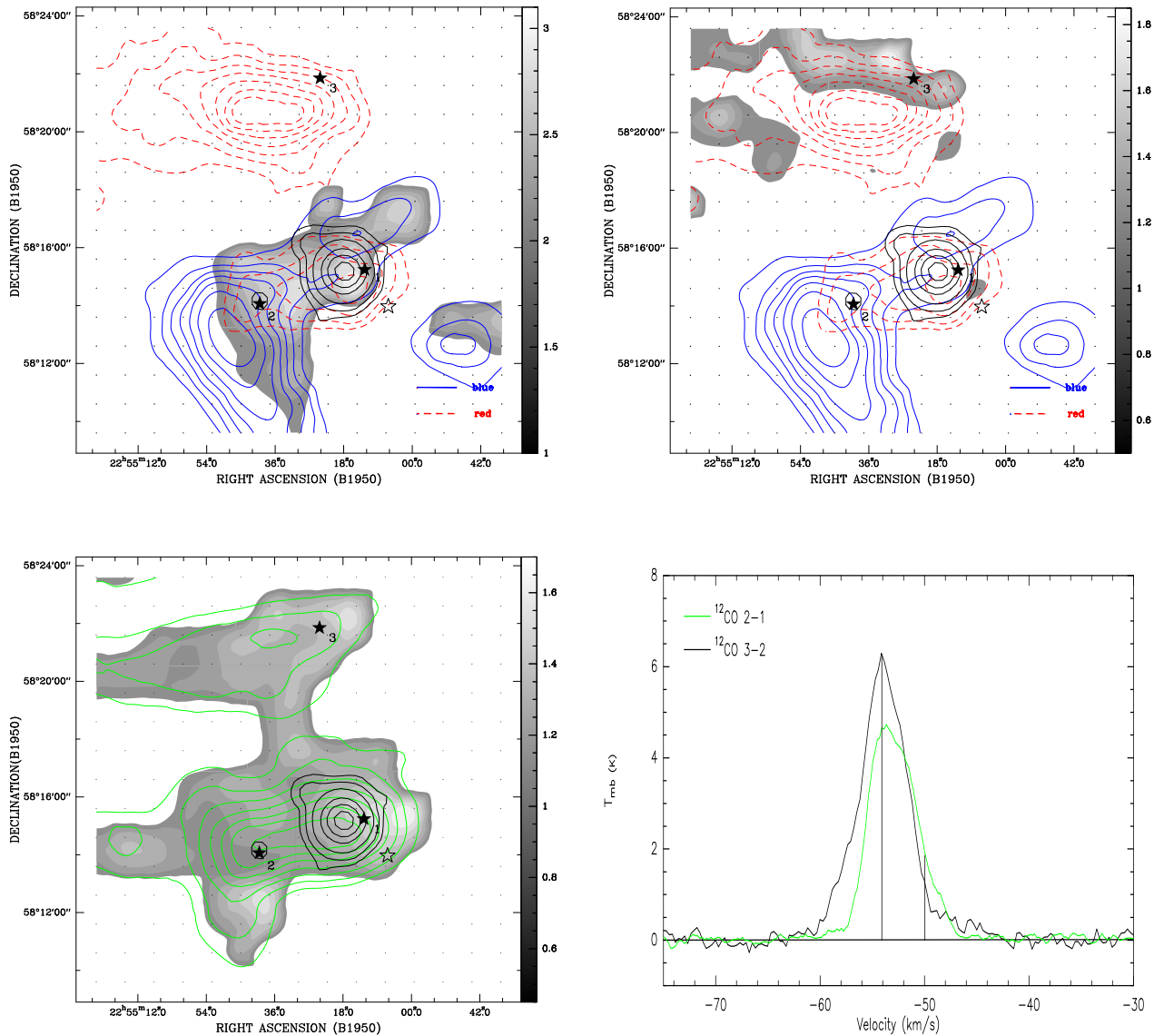


Fig. B.10. S149. Top-left panel: outflow contours (blue and red-shifted components are shown as blue solid and red dashed lines) are superimposed on the line intensity ratio map (grey scale) of the blue wing. Top-right panel: outflow contours are superimposed on the line intensity ratio map (grey scale) of the red wing. Bottom-left panel: the integrated intensity map of the core in CO $J = 2 - 1$ (green solid contours) are superimposed on the grey map of the line intensity ratio from the core component. The thin solid lines show the continuum at 1.4 GHz from NVSS. The contours for the cores begin at 30% of the maximum integrated intensity I_{max} and increase at a step of 10% of I_{max} , and the integrated line intensity ratios range from 30% of the maximum $R_{\text{I}_{\text{CO}(3-2)}/\text{I}_{\text{CO}(2-1)}}$ to the maximum $R_{\text{I}_{\text{CO}(3-2)}/\text{I}_{\text{CO}(2-1)}}$. The intensity ratios indicate the gas temperature variations at different positions. The filled star 1, 2, 3 are IRAS 22542+5815, IRAS 22546+5814 and IRAS 22543+5821; the unfilled star is O8-type star SH2-148. Bottom-right panel: the spectra averaged over the outflow zones (the CO $J = 3 - 2$ data were smoothed to the resolution of the $J = 2 - 1$ observations); the vertical lines indicate the beginning of the blue and red wings.

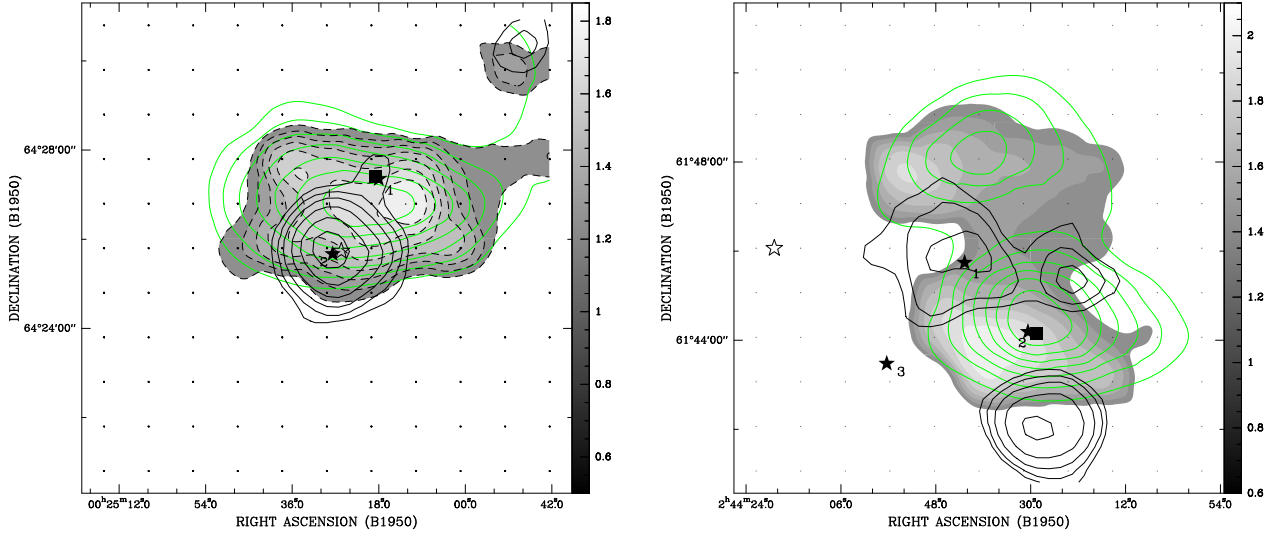


Fig. B.11. Left panel for S175: the integrated intensity map of the core in CO $J = 2 - 1$ (green solid contours) are superimposed on the grey map of the line intensity ratio from the core component, and the dashed contours are the integrated intensity map of the core in $^{13}\text{CO } J = 2 - 1$ line. The thin solid lines show the continuum at 1.4 GHz from NVSS. The filled stars 1 and 2 are IRAS 00243+6427 and IRAS 00244+6425, respectively. The unfilled star is O9.5 star ALS 6206. Right panel for S193: the integrated intensity map of the core in CO $J = 2 - 1$ (green solid contours) are superimposed on the grey map of the line intensity ratio from the core component. The thin solid lines show the continuum at 1.4 GHz from NVSS. The contours for the cores begin at 30% of the maximum integrated intensity I_{max} and increase at a step of 10% of I_{max} , and the integrated line intensity ratios range from 30% of the maximum $R_{I_{\text{CO}(3-2)}/I_{\text{CO}(2-1)}}$ to the maximum $R_{I_{\text{CO}(3-2)}/I_{\text{CO}(2-1)}}$. The intensity ratios indicate the gas temperature variations at different positions. The filled stars 1, 2 and 3 are IRAS 02437+6145, IRAS 02435+6144 and IRAS 02439+6143, respectively. The unfilled star is B4-type star GSC 04051-01677.

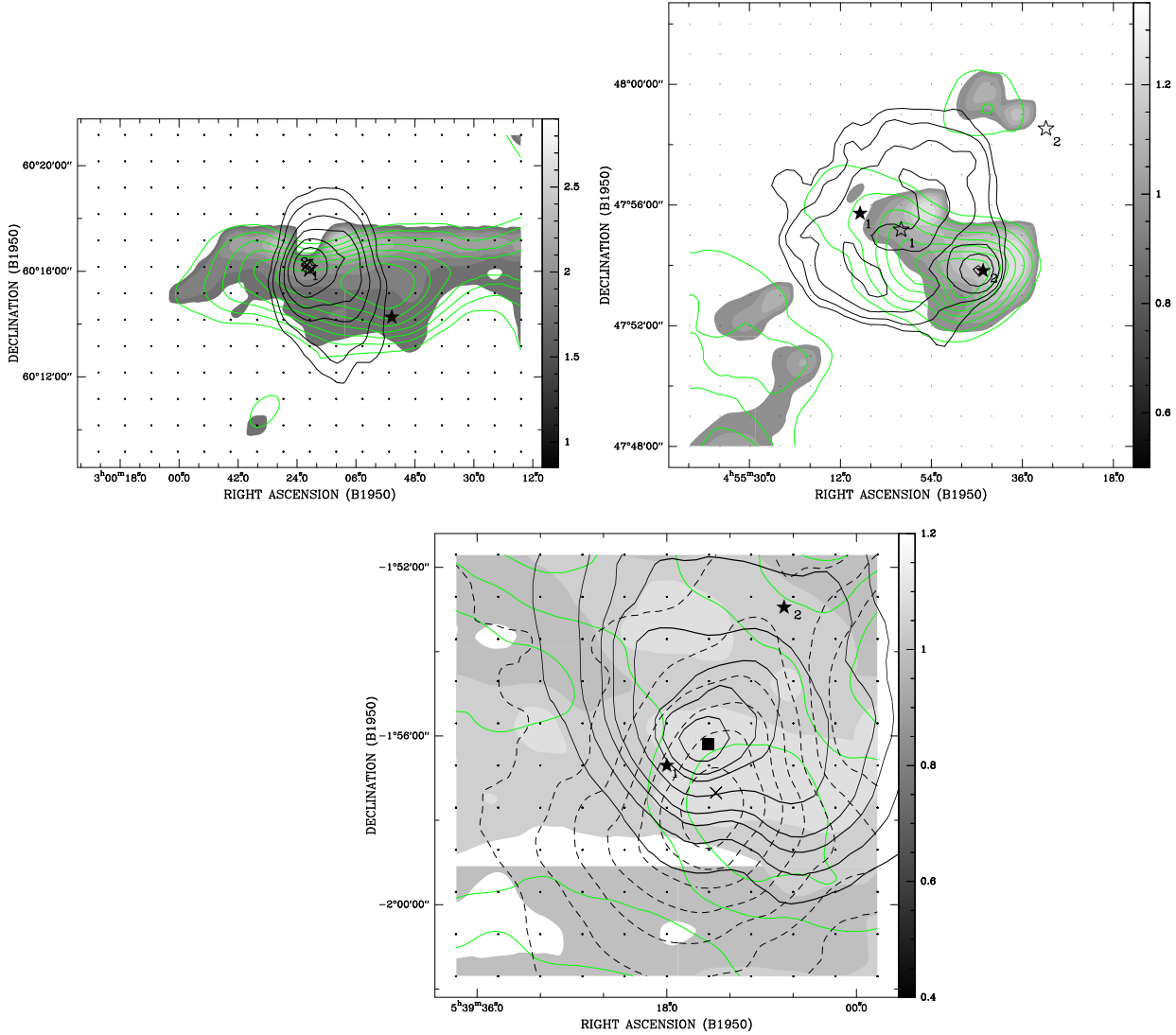


Fig. B.12. Left panel for S201: the integrated intensity map of the core in CO $J = 2 - 1$ (green solid contours) are superimposed on the grey map of the line intensity ratio from the core component. The thin solid lines show the continuum at 1.4 GHz from NVSS. The star is IRAS 02589+6014, the cross symbols 1 and 2 indicate the H₂O masers. IRAS 02593+6016 is overlaid at the maser 1 position. Right panel for S217: the integrated intensity map of the core in CO $J = 2 - 1$ (green solid contours) are superimposed on the grey map of the line intensity ratio from the core component. The thin solid lines show the continuum at 1.4 GHz from NVSS. The filled stars 1 and 2 are IRAS 04551+4755 and IRAS 04547+4753; the unfilled stars 1 and 2 are O9.5-type star LSV 47°24 and B8-type star BD+47 1079. Bottom panel for G206.543-16.347: the integrated intensity map of the core in CO $J = 2 - 1$ (green solid contours) are superimposed on the grey map of the line intensity ratio from the core component, and the dashed contours are the integrated intensity map of the core in ¹³CO $J = 2 - 1$ line. The thin solid lines show the continuum at 1.4 GHz from NVSS. The contours for the cores begin at 30% of the maximum integrated intensity I_{max} and increase at a step of 10% of I_{max} , and the integrated line intensity ratios range from 30% of the maximum $R_{I_{\text{CO}(3-2)}/I_{\text{CO}(2-1)}}$ to the maximum $R_{I_{\text{CO}(3-2)}/I_{\text{CO}(2-1)}}$. The intensity ratios indicate the gas temperature variations at different positions. The stars 1 and 2 are IRAS 05393-0156 and IRAS 05391-0152, the cross symbol mark H₂O maser.

References

- Argon, A.L., Reid, M.J. & Menten, K.M. 2000, *ApJS*, 129, 159
- Arquilla, R. & Goldsmith, P. F. 1984, *ApJ*, 279, 664
- Bachiller, R. 1996, *ARA&A*, 34, 111
- Benson, P.J., Little-Marenin, I.R., Woods, T.C., et al. 1990, *ApJS*, 74, 911
- Beuther, H., Schilke P., Sridharan, T.K., et al. 2002, *A&A*, 383, 892
- Bontemps, S., Andre, P, Terebey, S., et al. 1996, *A&A*, 311, 858
- Casoli, F., Combes, F. & Dupraz, C. 1986, *A&A*, 169, 281
- Caswell, J.L., Yi, J., Booth, R.S., et al. 2000, *MNRAS*, 313, 599
- Cesaroni, R., Palagi, F. & Felli, M. 1988, *A&AS*, 76, 455
- Choi, M., Evans II, N.J. & Jaffe, D.T. 1993, *ApJ*, 417, 624
- Churchwell, Ed. 2002, *ARA&A*, 40, 27
- Codella, C., Testi, L. & Cesaroni, R. 1997, *A&A*, 325, 282
- Cohen, M. & Green, A.J. 2001, *MNRAS*, 325, 531
- Condon, J.J., Cotton, W.D., Greisen, E.W., et al. 1998, *AJ*, 115, 1693
- Correia, J.C., Griffin, M. & Saraceno, P. 1997, *A&A*, 322, L25
- Cragg, D.M., Sobolev, A.M. & Godfrey, P.D. 2002, *MNRAS*, 331, 521
- Deharveng, L., Zavagno, A., Nadeau, D., et al. 1999, *A&A*, 344, 943
- Deharveng, L., Zavagno, A., Salas, L., et al. 2003, *A&A*, 399, 1135
- Deharveng, L., Zavagno, A. & Caplan, J., et al. 2005, *A&A*, 433, 565
- Elitzur, M., Hollenbach, D.J. & McKee, C.F. 1989, *ApJ*, 346, 983
- Felli, M., Hjellming, R.M. & Cesaroni, R. 1987, *A&A*, 182, 313
- Felli, M., Palagi, F. & Tofani, G. 1992, *A&A*, 255, 293
- Fich, M. 1993, *ApJS*, 86, 497
- Garay, G. & Lizano, S. 1999, *PASP*, 111, 1049
- Garden, P.R., Hayashi, M., Gatley, I., et al. 1991, *ApJ*, 374, 540
- Goldreich, P. & Kwan, J. 1974, *ApJ*, 189, 441
- Goldsmith, P.F., Snell, R.L., Hemeon-Heyer, M., et al. 1984, *ApJ*, 286, 599
- Gomez, Y., Lebron, M., Rodriguez, L.F., et al. 1998, *ApJ*, 503, 297
- Gomez, Y., Rodriguez, L.F. & Garay, G. 2000, *ApJ*, 531, 861
- Harju, J., Lehtner, K., Booth, R., et al. 1998, *A&AS*, 132, 211
- Hasegawa, T.I., Mitchell, G.F., Matthews, H.E., et al. 1994, *ApJ*, 426, 215
- Heaton, B.D., Andersson, M., Dent, W.R.F., et al. 1988, *A&A*, 203, 99
- Henkel, C., Haschick, A.D., Gusten, R., et al. 1986, *A&A*, 165, 197
- Henning, T., Cesaroni, R., Walmsley, M., et al. 1992, *A&AS*, 93, 525
- Heyer, M.H., Snell, R.L., Morgan, J., et al. 1989, *ApJ*, 346, 220
- Johansson, L.E.B., Olofsson, H., Hjalmarson, A., et al. 1994, *A&A*, 291, 89
- Kaufman, M.J., Wolfire, M.G., Hollenbach, D.J., et al. 1999, *ApJ*, 527, 795
- Kim, Kee-Tae & Koo, Bon-Chul 2002, *ApJ*, 575, 327
- Kurtz, S., Churchwell, Ed. & Wood, D.O.S. 1994, *ApJS*, 91, 659
- Lada, C.J. 1985, *ARA&A*, 23, 267
- Langer, W. & Penzias, A., 1990, *ApJ*, 357, 477
- Leger, A. & Puget, J.L. 1984, *A&A*, 137, L5
- Marti, J., Rodriguez, L. F. & Reipurth, B. 1998, *ApJ*, 502, 337
- Palagi, F., Cesaroni, R. & Comoretto, G. 1993, *A&AS*, 101, 153
- Panagia, N., 1973, *AJ*, 78, 929
- Persi, P. & Tapia, M. 2003, *A&A*, 406, 149
- Rodriguze, L.F., Moran, J.M., Gottlieb, E.W., et al. 1980, *ApJ*, 235, 845
- Roger, R.S. & Leahy, D.A. 1993, *AJ*, 106, 31
- Sanders, D.B. & Willner, S.P. 1985, *ApJ*, 293, L39
- Shepherd, D. S. & Churchwell, Ed. 1996a, *ApJ*, 457, 267
- Shepherd, D. S. & Churchwell, Ed. 1996b, *ApJ*, 472, 225
- Shirley, Y.L., Evans II, N.J., Yang, K.E., et al. 2003, *ApJS*, 147, 375
- Shu, F.H., Ruden, S.P., Lada, C.J., et al. 1991, *ApJ*, 370, L31
- Tofani, G., Felli, M. & Faylor, G.B. 1995, *A&AS*, 112, 299
- White, G.J. & Gee G., 1986, *A&A*, 156, 301
- Wilson, C.D., Walker, C.E. & Thornley, M.D. 1997, *ApJ*, 483, 210
- Wilson, C.D., Howe, J.E. & Balogh, M.L. 1999, *ApJ*, 517, 174
- Wood, D.O.S. & Churchwell, Ed. 1989, *ApJS*, 69, 831
- Wouterloot, J.G.A. & Brand, J. 1989, *A&AS*, 80, 149
- Wu, Y., Wei, Y., Zhao, M., et al. 2004, *A&A*, 426, 503
- Wu, Y., Zhang, Q., Chen, H., et al. 2005, *AJ*, 129, 330
- Wynn-Williams, C.G., Becklin, E.E., Beichman, C.A., et al. 1981, *ApJ*, 246, 801
- Zinchenko, I., Forsstrom, V., Lapinov, A., et al. 1994, *A&A*, 288, 601

Table 1. Observation Log. The columns give source name, coordinates^a, transitions, number of mapped points, rms of spectra, system temperatures.

Source	$\alpha(1950)$ (h m s)	$\delta(1950)$ ($^{\circ}$ ' ")	Transitions	Pos.	T_{mb}^{rms} (K)	T_{sys} (K)
S175	00 24 28.8	64 25 48	CO(2 – 1)	121	0.18	160
			CO(3 – 2)	121	0.37	285
			¹³ CO(2 – 1)	121	0.18	221
S186	01 05 38.3	62 51 36	CO(2 – 1)	121	0.18	180
			CO(3 – 2)	121	0.41	306
			¹³ CO(2 – 1)	121	0.08	173
S193	02 43 39.8	61 46 04	CO(2 – 1)	121	0.16	180
			CO(3 – 2)	121	0.28	282
S201	02 59 20.1	60 16 10	CO(2 – 1)	221	0.24	195
			CO(3 – 2)	221	0.71	280
G139	03 03 33.0	58 19 21	CO(2 – 1)	121	0.25	158
			CO(3 – 2)	121	0.48	282
S217	04 55 00.0	47 55 00	CO(2 – 1)	225	0.2	171
			CO(3 – 2)	225	0.46	287
G206	05 39 18.0	–01 56 42	CO(2 – 1)	121	0.53	175
			CO(3 – 2)	121	1.34	295
			¹³ CO(2 – 1)	121	0.28	194
G189	06 06 23.0	20 40 02	CO(2 – 1)	121	0.21	167
			CO(3 – 2)	121	0.43	273
			¹³ CO(2 – 1)	121	0.09	172
G213	06 08 24.5	–06 11 12	CO(2 – 1)	121	0.30	173
			CO(3 – 2)	121	0.70	288
			¹³ CO(2 – 1)	121	0.26	201
G192	06 09 57.9	18 00 12	CO(2 – 1)	441	0.26	181
			CO(3 – 2)	441	0.56	296
S288	07 06 11.0	–04 13 00	CO(2 – 1)	121	0.26	189
			CO(3 – 2)	121	0.73	321
G70	19 59 50.0	33 24 20	CO(2 – 1)	121	0.16	139
			CO(3 – 2)	121	0.25	237
S127	21 27 04.6	54 23 20	CO(2 – 1)	121	0.13	149
			CO(3 – 2)	121	0.27	246
S138	22 30 52.6	58 12 48	CO(2 – 1)	121	0.22	168
			CO(3 – 2)	121	0.55	299
			¹³ CO(2 – 1)	121	0.09	163
S149	22 54 14.5	58 16 36	CO(2 – 1)	225	0.24	173
			CO(3 – 2)	225	0.47	286

^aCentral coordinates of the maps.

Table 2. Velocity intervals and maximum integrated intensities for the maps presented in Figs.1-12^a.

Source	Δv_b (km s ⁻¹)	$I_{\max}(b)$ (K km s ⁻¹)	Δv_r (km s ⁻¹)	$I_{\max}(r)$ (K km s ⁻¹)	Δv_c (km s ⁻¹)	$I_{\max}(c)$ (K km s ⁻¹)	$I_{\max}(13)$ (K km s ⁻¹)
S175					(-52, -46)	28	6
S186	(-46, -44)	4	(-42, -38)	5	(-44, -42)	15	5
S193					(-51, -42)	23	
S201					(-52, -46)	28	
G139	(-46, -41)	38	(-38, -33)	25	(-41, -38)	65	
S217					(-24, -14)	41	
G206					(0, 21)	217	91
G189	(0, 8)	32	(10, 15)	15.7	(8, 10)	33	16
G213	(2, 8)	11	(16, 22)	10	(8, 16)	81	37
G192	(3, 6)	27	(10, 13)	19	(6, 10)	95	
S288	(52, 56)	5.6	(57, 60)	6.2	(56, 57)	4.8	
G70	(-35, -26)	34	(-21, -12)	28	(-26, -21)	83	
S127	(-100, -95)	6.4	(-93, -88)	4	(-95, -93)	7.5	
S138	(-65, -54)	20	(-50, -39)	19	(-54, -50)	19	15
S149	(-60, -54)	25	(-50, -44)	14	(-54, -50)	41	

^aThe maximum integrated intensities (I_{\max}) in $^{12}\text{CO } J = 2 - 1$ and their corresponding integrated velocity ranges (Δv); b, r and c indicate the blue, red-shifted outflow and core components, respectively. $I_{\max}(13)$ indicate the maximum integrated intensities of the cores in $^{13}\text{CO } J = 2 - 1$, the cores in $^{13}\text{CO } J = 2 - 1$ have same integrated velocity range as those in $^{12}\text{CO } J = 2 - 1$.

Table 3. Physical Parameters of Outflows.

Source	M (M_{\odot})	P ($M_{\odot} \text{ km s}^{-1}$)	E (10^{46} erg)	t (10^4 yr)	\dot{M}_{loss} ($10^{-4} M_{\odot} \text{ yr}^{-1}$)	F_m ($10^{-3} M_{\odot} \text{ km s}^{-1} \text{ yr}^{-1}$)	L_m (L_{\odot})
S186	83	255	7	1.7	0.3	14	3
G139	481	2575	12	0.7	7.4	366	138
G189	384	2024	11	0.3	13.5	660	288
G213	11	123	11	0.1	2.5	90	684
G192	170	1172	7	1.2	1.9	1200	48
S288	33	94	2.7	0.9	0.2	9	2
G70	1045	8778	65	1.8	9.7	490	300
S127	1021	2329	9.2	6.1	0.7	126	12
S138	840	7875	68	0.7	22.5	1272	870
S149	764	5265	31	2.5	4.2	210	102

Table 4. The Identifications^a of the associated stellar objects, NVSS continuum, 8.3 μm emission and line intensity ratio with the HII complexes.

Source	D (kpc)	IRAS/stars	L ($10^3 L_{\odot}$)	ST	NVSS	P_{MSX} (" , ")	R_b	R_r	R_c
S175	1.7	IRAS 00244+6425	1.9	B3	Y	(7.9,6.5)			-
		IRAS 00243+6427	0.21	ML	N	(0.0,0.0)			+
		ALS6206		O9.5	N				
S186	4.0	IRAS 01056+6251	11.4	B0.5	Y	(26.6,17.6)	+	+	+
		IRAS 01053+6251	1.49	B3	N	(6.5,18.7)	+	+	+
S193	5.2	IRAS 02435+6144	1.2	B3	N	(-11.1,-0.4)			+
		IRAS 02437+6145	5.4	B2	Y				
		IRAS 02439+6143	0.33	ML	N				
		GSC 04051-01677		B4	N				
S201	4.0	IRAS 02593+6016	56	O8.5	Y	(23.3,10.1)			+
		IRAS 02598+6014	50	O9	N	(9.7,7.9)			-
G139	4.2	IRAS 03035+5819	67	O8	Y	(-24.8,-2.9)	+	+	+
		IRAS 03037+5819	9.6	B0.5	N	(-11.8,-7.2)	-	-	-
S217	2.8	IRAS 04547+4753	8.7	B0.5	Y	(0.0,0.0)			+
		IRAS 04551+4755	1.76	B3	N				
		LSV 47°24		O9.5	N				
		BD+47 1079		B8	N				
G206	0.5	IRAS 05393-0156	13	B0.5	Y	(0.0,0.0)			+
		IRAS 05391-0152	1.96	B3	N	(0.0,0.0)			-
G189	2.8	IRAS 06063+2040	28	B0	Y	(-28.4,5.7)	+	+	+
		ALS 8745		B	N				
		ALS 8748		B	N				
		HD 252325		B1	Y				
G213	1.0	IRAS 06084-0611	11	B0.5	Y	(0.0,0.0)	+	-	+
G192	2.5	IRAS 06099+1800	61	O8.5	Y	(11.2,3.6)	+	+	-
		IRAS 06096+1757	21.9	B0.5	Y	(0,0)	-	-	-
		IRAS 06105+1756	7.6	B1	Y				
		HD253327		B0.5	Y				
		HD253247		B1	Y				
S288	7.2	IRAS 07061-0414	78	O8	Y	(-2.5,1.1)	-	+	-
		HD 296489		B8	N				
G70	8.6	IRAS 19598+3324	228	O4	Y	(0.0,0.0)	+	+	+
S127	11.5	IRAS 21270+5423	100	O7	Y	(21.6,42.8)	+	-	+
						(-24.1,-19.8)	-	+	+
S138	5.7	IRAS 22308+5812	84	O7.5	Y	(-3.6,-2.5)	+	-	+
		GRS105.63-00.34		O7.5	Y	(1.3, -2.4)	+	-	+
S149	5.5	IRAS 22542+5815	48	O9	Y	(-9.0,0.4)	+	-	+
		IRAS 22543+5821	2.6	B3	N				
		IRAS 22546+5814	4.3	B2	N				
		SH2-148		O8	N				

^aThe distance (D) is from Kurtz, Churchwell & Wood (1994) and Wouterloot & Brand (1989). The far-infrared luminosity (L) is derived based on the formula of Casoli, Combes & Dupraz (1986). The corresponding spectral type (ST) of the far-infrared luminosity (L) is referred to the work of Panagia (1973); the spectral type of the massive stars is taken from SIMBAD database. ML marks intermediate or low mass star. P_{MSX} presents the offset (arcsec) of MSX sources relative to IRAS sources. R_b , R_r and R_c indicate the maximum intensity ratios determined from the blue-shifted and red-shifted wings of the outflow and core component, respectively, as shown in the wedges of the Figs.B.1-12. The plus symbol indicates that the MSX sources are associated with the maximum ratios (R_b , R_r and R_c). The minus symbol indicates that the MSX sources are not related to the maximum ratios.